Published in final edited form as:

Dev Biol. 2017 December 01; 432(1): 98–124. doi:10.1016/j.ydbio.2017.08.026.

Visceral endoderm and the primitive streak interact to build the fetal-placental interface of the mouse gastrula

Adriana M. Rodriguez and **Karen M. Downs***

Department of Cell and Regenerative Biology, University of Wisconsin-Madison School of Medicine and Public Health, 1300 University Avenue, Madison, WI 53706 USA

Abstract

Hypoblast/visceral endoderm assists in amniote nutrition, axial positioning and formation of the gut. Here, we provide evidence, currently limited to humans and non-human primates, that hypoblast is a purveyor of extraembryonic mesoderm in the mouse gastrula. Fate mapping a unique segment of axial extraembryonic visceral endoderm associated with the allantoic component of the primitive streak, and referred to as the “AX”, revealed that visceral endoderm supplies the placentae with extraembryonic mesoderm. Exfoliation of the AX was dependent upon contact with the primitive streak, which modulated Hedgehog signaling. Resolution of the AX’s epithelial-to-mesenchymal transition (EMT) by Hedgehog shaped the allantois into its characteristic projectile and individualized placental arterial vessels. A unique border cell separated the delaminating AX from the yolk sac blood islands which, situated beyond the limit of the streak, were not formed by an EMT. Over time, the AX became the hindgut lip, which contributed extensively to the posterior interface, including both embryonic and extraembryonic tissues. The AX, in turn, imparted antero-posterior (A-P) polarity on the primitive streak and promoted its elongation and differentiation into definitive endoderm. Results of heterotopic grafting supported mutually interactive functions of the AX and primitive streak, showing that together, they self-organized into a complete version of the fetal-placental interface, forming an elongated structure exhibiting A-P polarity that was composed of the allantois, a rod-like axial extension reminiscent of the embryonic notochord, the placental arterial vasculature and visceral endoderm/hindgut.

Keywords

allantois; epithelial-to-mesenchymal transition; extraembryonic mesoderm; Hedgehog; hypoblast; primitive streak

INTRODUCTION

Together with reptiles and birds, mammals are part of the broad group, Amniota. In their transition to life on land, amniotes evolved a set of conserved extraembryonic tissues, often called “fetal membranes”, among which the allantois, chorion, yolk sac, and amnion collaborate to sustain embryo survival within the egg or maternal reproductive tract. In

*Correspondence and requests for materials should be addressed to K.M.D: (kdowns@wisc.edu).

Placentalia, the fetal bloodstream was co-opted by these extraembryonic tissues, which form two major placentae: chorio-allantoic and chorio-vitelline (yolk sac) (reviewed in (Downs, 2004)). Together, the vasculatures of these placentae unite with those of the fetus, thereby enabling the transport of fetal blood to and from the chorion to permit fetal-maternal exchange.

The chorio-allantoic placenta is composed of the trophoblast-derived chorionic disk and the allantois-derived umbilical cord. The chorio-vitelline placenta is composed of trophoblast-derived tissues and the yolk sacs, both visceral and parietal. Each placenta establishes its own umbilical and omphalomesenteric circulatory systems, respectively, and each placenta is hematopoietic (Gekas et al., 2005; Gekas et al., 2010; Otterbach and Dzierzak, 2005; Palis, 2001; Zeigler et al., 2006), further boosting the fetus' dowry of blood cells during gestation. Together with the fetal cardiovascular dorsal aortae, the umbilical and omphalomesenteric arteries unite along the axial midline, thereby contributing to directed and efficient flow of blood to and from the mother. Key to this continuum is the allantois, or pre-umbilical cord.

The allantois is an outcropping of the posterior end of the embryo. In the gastrulating mouse, the allantois forms a small mesodermal bud that is ultimately transformed into a sausage-shaped projectile, reaching toward the chorion and fusing with it to create the labyrinth of the chorio-allantoic placenta, where exchange takes place with the mother. Within the base of the allantois, closest to the embryo, a special hemogenic vascular branchpoint forms in register with the embryo's body axis, the primitive streak (Daane et al., 2011; Daane and Downs, 2011; Downs et al., 1998). This "vessel of confluence" unites the major arterial vessels of the independently formed umbilical, vitelline and embryonic cardiovascular systems in all Placentalia thus far examined (Daane and Downs, 2011; Downs et al., 1998; Rodriguez et al., 2017).

When considering the chorio-allantoic and chorio-vitelline placentae and their relationship to the fetus, the primitive streak rarely comes to mind, if at all. The primitive streak is the overt manifestation of antero-posterior (A-P) polarity of the embryo. It is an axial mesendodermal progenitor tissue that creates and delivers the three primary germ layers, especially mesoderm and definitive endoderm, in organized manner to the fetus during gastrulation (Kinder et al., 1999; Tam and Beddington, 1987).

The textbook view is that the primitive streak is confined to the embryo proper (Downs, 2009). Unexpectedly, however, after completing elongation through the embryo, the streak's posterior end reaches into the extraembryonic region where, within the base of the allantois, it expands into a dense core, the allantoic core domain (ACD) (Downs et al., 2009). Microsurgical removal of the ACD revealed a role in allantoic elongation to the chorion (Downs et al., 2009), while fate mapping showed that, like the embryonic posterior primitive streak (Downs et al., 2009; Kinder et al., 1999; Lawson et al., 1991; Snell and Stevens, 1966; Tam and Beddington, 1987), the ACD contains precursors of all three germ layers, delivering them to the fetal-placental interface, and building the allantois (Mikedis and Downs, 2012). Recently, we have shown that the ACD organizes the formation of the allantois's vessel of confluence (Rodriguez et al., 2017), thereby creating the arterial

continuum that unifies the embryo and its placentae through a common axial site. Moreover, a dense allantoic core is conserved amongst those Placentalia examined thus far (Rodriguez et al., 2017).

Although the embryonic posterior primitive streak contributes mesoderm to the allantois, above, whether the streak, both embryonic and extraembryonic components, provides the allantois with its full complement of mesoderm is not known. For example, given that the streak extends into the exocoelom, it is difficult to envision a mechanism by which epiblast, confined to the embryonic region, can ingress into this extraembryonic streak and become mesoderm. Rather, provision of extraembryonic mesoderm to the allantois by adjacent visceral endoderm might anatomically make more sense. Moreover, it is thought that proliferation kinetics are incompatible with the streak acting as a stem cell population that exfoliates the entire mesoderm (Snow, 1977), though this possibility was never further explored.

In humans and non-human primates, extraembryonic mesoderm has a binary origin within both the epiblast and hypoblast. Primitive endoderm, or “hypoblast” in humans supplies extraembryonic mesoderm to the placentae in advance of the appearance of the streak (Bianchi et al., 1993; Enders and King, 1988). Although the mechanism by which human hypoblast is converted into mesoderm is not known, mesodermal lineage differences between rodents and other placental mammals, if true, have limited the full translational utility of the mouse model to human development, particularly placentation, abnormalities of which are often fatal, or result in severe birth defects (Cullen, 1916; Stevenson and Hall, 2006).

In the mouse, primitive endoderm and epiblast segregate from each other at implantation (Gardner, 1982; Gardner and Rossant, 1979). Subsequently, primitive endoderm becomes visceral and parietal endoderm, whose primary roles, historically, are nutritive (Snell and Stevens, 1966). Results of more recent studies have, however, shown that visceral endoderm, a simple epithelium, contributes to definitive gut endoderm (Kwon et al., 2008), and that it has inducing roles that extend to the yolk sac blood islands (Belaoussoff et al., 1998) and forebrain (Thomas and Beddington, 1996). In addition, signaling from the prospective forebrain’s associated anterior visceral endoderm, or AVE, is thought to position the primitive streak to the posterior side of the embryo (Stower and Srinivas, 2014).

None of these studies entertained the possibility that extraembryonic visceral endoderm, i.e., that associated with the allantois and yolk sac, might be a source of mesendoderm. Some years ago, two anecdotal pieces of data appeared in the literature, which suggested to us that this might be the case. Jurand presented a tantalizing image, without explanation or attribution, of extraembryonic visceral endoderm bifurcating from the yolk sac into the allantois, where it formed a rod-like extension (Downs, 2009; Jurand, 1974). These bifurcations are reminiscent of the yolk sac diverticulum, which is thought in humans to form the scaffold upon which the body stalk/allantois is elaborated (O’Rahilly, 1973). In another report, creation of tetraploid mouse conceptuses produced a modest, albeit smaller-than-normal allantois which, though not noteworthy at the time (Tarkowski et al., 1977), is surprising in retrospect, as epiblast cannot maintain higher orders of ploidy, while visceral

endoderm and trophoblast can (Nagy, 1990). Moreover, this vestigial allantois, as well as that presented in a later study (Eakin et al., 2005), was associated with an embryonic hindgut structure, in accord with visceral endoderm's ability to contribute to gut endoderm (Dufort et al., 1998; Kwon et al., 2008). Although chimeras between 2N ⟷ 4N tissue could have addressed the possibility of visceral endoderm contribution to the allantois and other placental tissues, such contribution or lack thereof was not noted in that study (Eakin et al., 2005).

We had previously shown that cells expressing *Runx1*, which identifies hemangioblasts (North et al., 2002; North et al., 1999), form a continuous trail between allantois-associated extraembryonic visceral endoderm (henceforth referred to as "AX"; (Downs, 2008; Downs et al., 2009; Stern and Downs, 2012) and the allantois (Daane and Downs, 2011). While gene expression is not equivalent to cell lineage (Beddington, 1988), nevertheless, it can alert the investigator to that possibility, to be subsequently tested by unbiased fate mapping (Thomas et al., 1998). Continuity of *Runx1* expression between the AX and allantois suggested that the mouse allantois, like that of other Placentalia (Mossman, 1937), might contain an endoderm-derived component.

Other observations support this possibility. For example, the AX is part of a circumferential band of "transitional" visceral endoderm located at the embryonic-extraembryonic interface. Its morphology is intermediate between that of extraembryonic visceral endoderm, which surrounds the visceral yolk sac, and of embryonic visceral endoderm, which surrounds the epiblast (Bonnevie, 1950). The AX, which contains many fewer vacuoles and microvilli than columnar epithelium of the yolk sac (Downs et al., 2009), exhibits dynamic morphological changes, transitioning from a highly vesiculated simple columnar epithelium into a squamous one (Downs et al., 2009). This transition occurs concomitantly with breakdown in the extracellular matrix between it and the underlying allantois (Mikedis and Downs, 2009), suggesting the possibility of free cellular passage between these tissues. Many proteins characteristic of both mesoderm and endoderm have been detected in the AX (Downs, 2008; Downs et al., 2009; Mikedis and Downs, 2012, 2013, 2017; Wolfe and Downs, 2014; Wolfe et al., 2017) as well as in mouse XEN cell lines, which are derived from extraembryonic visceral endoderm (Kunath et al., 2005). Together, these observations suggest the possibility that the visceral endoderm, or at least that associated with the allantois, might be a bipotential mesendodermal tissue.

Of extraembryonic visceral endoderm, the AX is unique in being the only region associated with the primitive streak. In accord with its axial position, *Patched1* (*Ptch1*), the major receptor of the Hedgehog signaling pathway (Ingham and McMahon, 2001), is expressed at both low and high levels within axial allantois-associated visceral endoderm (Daane and Downs, 2011). The low *Ptch1* domain characterizes the AX, which is in contact with the primitive streak, while the high *Ptch1* domain encompasses a small segment of visceral endoderm contiguous with and immediately distal to the AX, henceforth called "distal AX" or dAX (Daane and Downs, 2011). Together with Hedgehog's involvement in organization around the axial midline during development (Ingham and McMahon, 2001), and a possible role in the epithelial-to-mesenchymal transition (EMT) reported at least in pathological scenarios (though not *in vivo*) (Karhadkar et al., 2004), we investigated the possibility that

the AX is a uniquely mesendodermal tissue whose bipotency is released by contact with the primitive streak. We fate mapped the AX in four ways. In the first, *in situ* DiI labeling the AX was followed by photobleaching (Sulik et al., 1994). In the second, this *in situ* labeling method was followed by fluorescence imaging (Beddington, 1994; Kinder et al., 1999; Thomas and Beddington, 1996; Thomas et al., 1998), particularly confocal analysis. Third, we orthotopically grafted the AX alone (Beddington, 1981, 1982), and followed its fate after staining for *lacZ* expression (Friedrich and Soriano, 1991), which is found in all cell types, both donor and host, during the stages of development examined here (Downs and Harmann, 1997). Finally, we genetically "lineage" traced, via Cre-inducible gene expression, the visceral endoderm-specific gene, transthyretin (Kwon et al., 2008).

MATERIALS AND METHODS

Animal husbandry, mouse strains, embryo dissections, and whole embryo culture

Animals were treated in accordance with Public Law 99-158 as enforced by the University of Wisconsin-Madison. Methods for timed matings, embryo dissections, and whole embryo culture were as previously described (Downs, 2006). The F2 of the standard inbred hybrid mouse strain (*B6CBAF1/J* F1) (The Jackson Laboratory, Bar Harbor, ME; stock number 100011) provided wildtype conceptuses, and/or were used to outbreed mice carrying genetic modifications. *Rosa26/26* mice (Friedrich and Soriano, 1991) were maintained as previously described (Downs and Harmann, 1997)*; Rosa26/26* males were bred with F1 females, above, and the resultant embryos were used as donor material in grafting experiments. *Ptch1:lacZ (Ptch1$^{tm1Mps/J}$)* reporter mice were maintained as heterozygotes, and male stud *Ptch1:lacZ* heterozygotes were mated with F1 females, above, with the resultant embryos used to identify the whereabouts of *Ptch1* expression, as previously described (Daane and Downs, 2011). *T-curtailed* (*T^{C}*) was maintained and genotyped as previously described (Inman and Downs, 2006b). Creation of the *T^{C}/Ptch1:lacZ* strain heterozygous for both alleles was carried out by mating *T^{C}/T^{+}* males with *Ptch1:lacZ* reporter females, and assaying ear punches from resultant tailless males for the presence of the *lacZ* gene (Daane and Downs, 2011). For assaying the relationship between the primitive streak and *Ptch1* expression in gastrulae, stud *T^{C}/Ptch1:lacZ* males were mated with *T^{C}/T^{+}* females, and resultant embryos dissected, X-gal stained (below), and genotyped by yolk biopsy as previously described (Inman and Downs, 2006b). For genetic lineage tracing experiments, hemizygous *Transthyretin-driven Cre recombinase* (*Ttr::Cre$^{Tg/+}$*) animals of breeding age were mated with wildtype *Ttr::Cre$^{+/+}$* (generous gift of Dr. K. Hadjantonakis) (Kwon et al., 2008). Ear punches from resultant pups were genotyped (http://www.ics-mci.fr/mousecre/static_page/procedures); results showed that they did not follow the expected 1:1 Mendelian ratio (79.4% *Ttr::Cre$^{Tg/+}$* vs 20.6% *Ttr::Cre$^{+/+}$*; Chi-square test with 1 degree of freedom, p<0.0001). Nevertheless, hemizygous *Ttr$^{Cre/+}$* females were mated with *CMV-Tomato-Green Fluorescent Protein (Tm/GFP)* homozygous males (Muzumdar et al 2007) (Jackson Laboratory) to produce *Ttr::Cre$^{Tg/+}$*;Tm/GFP. Yolk sac biopsies were taken (~E8.5-E9.0; 2 litters; n=22 conceptuses), genotyped (http://www.ics-mci.fr/mousecre/static_page/procedures), and found to follow the expected 1:1 Mendelian ratio (59.1% *Ttr::Cre$^{Tg/+}$* vs 40.9% *Ttr::Cre$^{+/+}$*; Chi-square test with 1 degree of freedom, p=0.3938). Thus, genetic background may play a role in ensuring correct segregation frequencies in such transgenic

mice. To ascertain contribution to internal tissues, conceptuses were immunostained for GFP as described below. GFP immunostaining *Ttr::Cre*$^{+/+}$;Tm/GFP conceptuses provided negative controls.

Embryo staging and panel displays, and terminology used for extraembryonic visceral endoderm

Briefly, the following stages (Downs and Davies, 1993) and abbreviations at approximate (~) nominal days post coitum (E, embryonic day) were used: *Neural plate stages*: No allantoic bud (OB; ~E7.0), Early Bud (EB; ~E7.25), and Late Bud (LB; ~E7.5). *Headfold (HF) stages*: very Early Headfold (vEHF; ~E7.75) when headfolds were faintly visible/not fully defined, Early Headfold (EHF; ~E7.75) when headfolds were visible, and Late Headfold (LHF; ~E8.0) when the foregut was visible. *Somite stages*: 1-13s (~E8.25-9.25). Embryonic stages are indicated in the upper right of most panels.

For cultured specimens, initial and final stages are separated by "/", i.e. initial/final stage. For grafted cultured specimens, initial donor and host stages are separated by "/" followed by the final stage of the operated chimeric conceptus.

Anatomical coordinates are as follows: for all histological or optical sections and diagrams in sagittal profile, posterior is on the right; for transverse profiles, ventral is on the bottom; distal/proximal coordinates refer to the extraembryonic region and are based on proximity to the embryo's posterior end, with "proximal" being closest to the embryo.

The term "allantois-associated extraembryonic visceral endoderm" (AX) was previously defined (Downs, 2008), and will be used for that portion of the visceral endoderm in contact with the base of the allantois, or primitive streak/ACD, and which expresses relatively low *Ptch1* (Daane and Downs, 2011). "Distal allantois-associated extraembryonic visceral endoderm" (dAX) will be used for that segment of AX which becomes separated from the allantoic mesoderm to which it contributes, and which is robustly *Ptch1*-positive (Daane and Downs, 2011).

Fate Mapping by DiI and photobleaching

CM-DiI (1,1'dioctadecyl-3,3,3',3'-tetramethylindocarbocyanine perchlorate; C-7001, Molecular Probes, Eugene, OR; stock 1 mg/ml in absolute alcohol), a non-toxic lipophilic dye was used to fate map extraembryonic visceral endoderm, either the AX, the visceral endoderm associated with the yolk sac blood islands, or the extraembryonic visceral endoderm lateral to the AX. DiI was diluted 1/20 in 0.3M sucrose immediately before use. Following isolation of live mouse embryos from the maternal tissue (Downs, 2006), conceptuses were scrutinized for any small lacerations that may have occurred during dissection, especially near the target application site, and discarded. A small DiI-charged capillary (10-20 μm diameter opening; flame-polished) was applied to the apical surface of the axial visceral endoderm in a dissection microscope (~x 17.5 magnification) for approximately 5-10 seconds with the aid of a mouth-held aspirator (Beddington, 1994). Immediately after DiI application, brightfield and fluorescence (TRITC filter cube, 553/570nm excitation/emission; Semrock, Rochester, New York) images were taken of the labeled conceptuses with a Retiga 2000R camera (QImaging, Surrey, BC) attached to a

Nikon Ti-U inverted compound microscope (NIS Elements software; Nikon, Tokyo, Japan). Images were superimposed via NIS Elements. In every experiment, labeled specimens were either immediately fixed in 4% paraformaldehyde (PFA) (Downs, 2008) for 2 hours at 4°C or cultured for 4-24 hours alongside unlabeled control specimens, photographed as above, and then fixed in the same manner. After rinsing out the PFA with phosphate-buffered saline (PBS; Sigma Aldrich; St Louis, MO), specimens were prepared either for fluorescent optical imaging after a 15 min incubation with DAPI (D1306, Life Technologies, Fitchburg, WI; stock 5 mg/mL; 3/5000 dilution in PBS); for fluorescent optical imaging following immunofluorescent chemistry; or for photobleaching (Singleton and Casagrande, 1996). For the latter, specimens were dehydrated up to and through 75% methanol in PBS before being exposed to 5% H2O2 in absolute methanol for 15-30 min on a platform rocker to remove endogenous peroxidase activity. After rehydration back to PBS, which was used to prevent the formation of H2O2-induced gas bubbles in the specimens and avoid tissue damage, labeled and control unlabeled conceptuses were subsequently placed, one by one, in fresh diaminobenzoate (DAB; K3468; 1-5% biphenyl-3,3',4,4'-tetrayltetraammonium tetrachloride; DAKO, Carpinteria, CA). The DiI-labeled or equivalent unlabeled region was exposed to excitation in the dark in a Nikon inverted microscope (TRITC filter cube, above) at magnification x400 for 20 minutes, checking every few minutes to verify that the specimen had not moved. At the end of the photobleaching period, DiI fluorescence was eliminated. After another hour of fixation, the photobleached conceptuses were prepared for histology, as described below, to visualize anatomical contribution of DiI-labeled descendant cells to internal tissues. Unfortunately, even five hours of incubation in H_2O_2 did not remove non-specific background in the visceral endoderm of unlabeled controls (Fig. 2C), and thus, only internal tissues were scored for the presence of brown precipitate.

Grafting the ACD+AX and ACD or AX alone

Rosa26/+ heterozygous donor conceptuses and host F2 conceptuses were dissected on the 8th day of gestation and maintained in culture medium at 37°C under 6.2% CO2 until grafting. Embryos were staged, after which the donor embryo was opened with dissection forceps to expose the allantois. For removal of the ACD with its associated AX (ACD+AX), glass scalpels (Beddington, 1987) were used, and the ACD was separated from the distal allantois by transversely cutting it away at a distance of 220 μm from its point of contact with the AX (Downs et al., 2009). For removal of the ACD, the whole allantois was aspirated from its point of contact with the AX using a hand-pulled glass capillary affixed to a mouth aspirator (Downs, 2006), after which the proximal 220 μm of the allantois, the ACD, was cut away from the distal allantois as described above. To introduce the desired ACD or ACD+AX donor pieces into a host conceptus, a 28g needle was first used to pierce the left lateral yolk sac of the host, through which the ACD alone or ACD+AX was introduced via the same hand-pulled glass capillary described above (Downs, 2006). For ACD+AX grafts, the ACD was oriented so as to enter the exocoelom first, leaving the AX in contact with the yolk sac wall. For grafts of the AX alone, conceptuses were first rinsed in sterile tissue-grade PBS and placed into trypsin/pancreatin for 2 minutes on ice (Downs and Harmann, 1997). The enzymatic reaction was stopped in dissection medium, and the AX was dissected away from the allantois with the aid of glass scalpels. To ensure purity of the AX, it was mouth-aspirated up and down several times in a small bore microcapillary to

liberate it from any residual mesoderm. In preliminary experiments, the AX was placed individually into the exocoelom of hosts, and immediately fixed, X-gal-stained, and prepared for histology; these experiments verified purity of the AX (Fig. 9N). The AX was then placed orthotopically and synchronously into hosts. Operated conceptuses were cultured alongside unoperated ones to verify optimal growth and development; no abnormalities were observed in the unoperated or grafted specimens. Following culture, embryos were scored as previously described (Downs and Harmann, 1997) and prepared for X-gal staining and immunohistochemistry, below.

X-gal staining, immunohistochemistry (IHC) and immunofluorescence (IF)

X-gal staining was carried out in *Ptch1:lacZ* conceptuses as previously described for signal enhancement (Daane and Downs, 2011); for grafts, X-gal staining followed a standard protocol (Downs and Harmann, 1997). The following categories of conceptuses underwent IHC (Downs, 2008): F2 conceptuses, and the following strains after X-gal staining: *Ptch1:lacZ; T^{C}/Ptch1:lacZ*; and grafted conceptuses. The following categories of conceptuses underwent IF (Mikedis and Downs, 2013): F2 conceptuses; and DiI-labeled/non-photobleached F2 conceptuses.

Primary antibodies and their sources, stock concentrations, dilutions, and Research Resource Identifiers (RRIDs) were: CASPASE-3 (CASP3) (559565, BD Biosciences, San Jose, California; 0.5 mg/ml, rabbit monoclonal; 1/100 IHC dilution; RRID: AB_397274); COLLAGEN TYPE IV (COLIV) (ab19808, Abcam, Cambridge, MA; 1 mg/ml, rabbit polyclonal; 1/50 IF dilution; RRID: AB_445160); E-CADHERIN (E-CAD) (sc-7870, Santa Cruz Biotechnology, Santa Cruz, California; 200 μg/ml, rabbit polyclonal; 1/10 IF dilution; RRID: AB_2076666) and (sc-31020, Santa Cruz Biotechnology; 200 μg/ml, goat polyclonal; 1/10 IF dilution; RRID: AB_2076663); FOXa2 (sc-9187, Santa Cruz Biotechnology; 200 μg/ml, goat polyclonal; 1/30 IF dilution; RRID: AB_2104886); GREEN FLUORESCENT PROTEIN (GFP) (ab6673, Abcam; 1 mg/ml, goat polyclonal,; 1/150 IHC dilution; RRID: AB_305643); INDIAN HEDGEHOG (IHH) (ab39634, Abcam, 1 mg/ml, rabbit polyclonal; 1/10 IF dilution; RRID: AB_881366); Ki67 (ab15580, Abcam; 1 mg/ml, rabbit polyclonal; 1/100 IHC dilution; RRID: AB_805388); Na^{+}-K^{+} ATPase (ab76020, Abcam; 0.6 mg/ml, rabbit monoclonal; 1/50 IF dilution; RRID: AB_1310695); N-CADHERIN (N-CAD) (ab18203, Abcam; 0.3 mg/ml, rabbit polyclonal; 1/200 IHC dilution; RRID: AB_444317); PECAM-1 (AF3628, R&D Systems, Minneapolis, MN; 0.2 mg/ml, goat polyclonal; 1/500 IHC dilution, 1/50 IF dilution; RRID: AB_2161028); PATCHED-1 (PTCH1) (sc-6149, Santa Cruz Biotechnology; 200 μg/ml, goat polyclonal; 1/10 IF dilution; RRID: AB_2174039); SONIC HEDGEHOG (SHH) (ab19897, Abcam; 0.4 mg/ml, rabbit polyclonal; 1/10 IF dilution; RRID: AB_2301807); SNAIL (sc-10433, Santa Cruz Biotechnology; 200 μg/ml, goat polyclonal; 1/100 dilution; RRID: AB_2191872); Brachyury (T) (sc-17743, Santa Cruz Biotechnology; 200 μg/ml, goat polyclonal; 1/100 IHC dilution; RRID: AB_634980); TRANSTHYRETIN (TTR) (sc-13098, Santa Cruz Biotechnology; 200 μg/ml, rabbit polyclonal; 1/25 IF dilution; RRID: AB_2241313); ZO-1 (sc-8146, Santa Cruz Biotechnology; 200 μg/ml, goat polyclonal; 1/10-25 IF dilution; RRID: AB_2205517), whose apical staining resembled that obtained by similar confocal methods (Grosse et al., 2011). Secondary antibodies were: Donkey anti-rabbit (sc-2089, Santa Cruz

Biotechnology; 0.4 mg/ml; 1/500 IHC dilution; RRID: AB_641178); Donkey anti-goat (sc-2042, Santa Cruz Biotechnology; 0.4 mg/ml; 1/500 IHC dilution; RRID: AB_631726); Dylight 488-conjugated donkey anti-goat (ab96935, Abcam; 0.5 mg/ml; 1/100 IF dilution; RRID: AB_10679538); Dylight 488-conjagated donkey anti-rabbit (ab96919, Abcam; 0.5 mg/ml; 1/500 IHC dilution; RRID: AB_10679362); Dylight 650-conjugated donkey anti-goat (ab96938, Abcam; 0.5 mg/ml; 1/100 IF dilution; RRID: AB_10680099); Dylight 650-conjugated donkey anti-rabbit (ab98501, Abcam; 0.5 mg/ml; 1/100 IF dilution; RRID: AB_10676120).

Histology

Conceptuses were prepared for histology as previously described (Downs et al., 1998). Briefly, following immunostaining, conceptuses were post-fixed overnight in 4% paraformaldehyde, then rinsed in PBS and dehydrated through an increasing series of ethanols, cleared in HemoDe (Scientific Safety Solvents, Keller, TX), then embedded in paraffin wax, using a dissection microscope to orient the conceptuses. Histological sections were of 6 μm thickness; after dewaxing, specimens were counterstained in hematoxylin (Gill's No. 1 hematoxylin; Sigma Aldrich).

Trypan blue exclusion for detection of apoptosis

A stock solution of 0.4 % trypan blue (diamine blue 3B; Allied Chemical, New York, NY) in sterile PBS was warmed at 56°C for several minutes before diluting 1/1000 times in whole embryo culture medium; embryos were cultured for 60 minutes, rinsed in PBS, fixed in Bouin's fluid for 2 hours (4°C), and processed for histology as described above.

Fluorescent optical imaging and depth of analysis

Following DAPI incubation and subsequent washes in PBS or PBSST for IF specimens (Mikedis and Downs, 2013), the posterior embryonic-extraembryonic interface (ie. the allantois, its overlying yolk sac and the posterior half of the embryo) was isolated using fine forceps and a long scalpel, and then transferred into a drop of Aqua-mount (13800, Lerner Laboratories, Pittsburgh, PA) that was centrally placed on a gelatin-subbed glass slide. Once the desired frontal, posterior upward, orientation was achieved, a No. 1.5 cover-glass was gently applied to prevent disrupting the tissue's orientation. Prior to letting the slides set overnight in the dark at 4°C, a slight force was exerted on the cover-glass; this compression not only prevented the tissue from moving before the Aqua-mount solidified, but also maximized the amount of tissue that was within the optical depth of the microscope. Fluorescent optical imaging was performed using a Nikon A1R+ Confocal Microscope (W.M. Keck Laboratory for Biological Imaging, University of Wisconsin-Madison) with a CFI Plan Apo Lambda 20x objective as well as 60x oil objective, a pinhole size of 1-1.8 AU, and lasers at 408, 488, 561 and 638 nm wavelengths. Using the NIS Elements Confocal software images were acquired as Z-stacks of 1 μm step increments from the deepest optical slice where signal was detected (farthest from the cover-glass) to the 1st optical slice where signal was detected (closest to the cover-glass). As the total depth of these Z-stacks was limited to only 40-50 μm, a set of samples (n=3) that were imaged on the Nikon A1R+ Confocal Microscope were imaged on a Spectral Lifetime Multiphoton Microscope (Laboratory for Optical and Computational Instrumentation (LOCI), University of

Wisconsin-Madison) as well. However, while multiphoton systems often have better optical depth than confocal microscopes (Pantazis and Supatto, 2014), we found that the images acquired through both systems had the same depth and similar signal for the red, green and blue channels (data not shown). In addition, IF and DiI labeled specimens were imaged alongside minus primary and unlabeled control specimens; in these only a DAPI signal was found (data not shown). Also, as the DiI signal was often quite strong on the visceral endoderm, in five DiI labeled specimens and two unlabeled controls, the yolk sac was removed, and mounted and imaged separately from the allantois and posterior embryo; DiI was still found in the allantois of all labeled specimens (see Fig. 1J).

Pharmacological inhibition of Hedgehog signaling

Cyclopamine binds to Smoothened and abrogates downstream Hedgehog signaling (Chen et al., 2002). Previous studies indicated that KAAD-cyclopamine (3-Keto-N-aminoethyl-N'-aminocaproyldihdrocinnamoyl cyclopmanine, Molecular Weight 697.99; K171000, Toronto Research Chemicals) exhibited 10-20-fold higher potency than cyclopamine in inhibiting *lacZ* expression in $p2^{Ptch-/-}$ cells, with similar or lower toxicity (Perron et al., 2003; Tiapale et al., 2000). To determine which concentration of KAAD-cyclopamine (KAAD) would be least toxic to the embryos used in this study, we first determined which concentration of the KAAD vehicle, 95% ethanol, had no obvious effects on embryonic growth and morphology: 4 μl, 3 mg/ml, 0.4% v/v; 8 μl, 6.0 mg/ml, 0.8% v/v; 12 μl, 9.0 mg/ml, 1.2% v/v; 20 μl, 15.0 mg/ml 2.0% v/v. Compared with untreated controls, 4 μl (3 mg/ml, 0.4% v/v) ethanol exhibited no toxicity; by contrast, embryos cultured in 8 μl ethanol exhibited delayed somitogenesis (1-2s), those cultured in 12 μl ethanol exhibited poor blood flow and an underdeveloped heart, and those cultured in 20 μl ethanol were completely abnormal with uninterpretable morphology. The adverse affects of these alcohol concentrations on embryonic development were similar to those previously observed (Xu et al., 2005). Thus, a 25 mM stock solution of KAAD was made in 95% ethanol; 4 μl aliquots were stored at −20°C. We then determined the optimal concentration of KAAD that would eliminate X-gal staining in $Ptch1^{+/-}$ while maintaining normal overall morphology: 0.8 μl (20 μM), 2 μl (50 μM), 3 μl (75 μM), and 4 μl (100 μM) of KAAD was added to 1 ml culture medium just prior to introducing embryonic pairs at headfold-5s stages (~E8.0-8.5; n=4 experiments). Conceptuses in each KAAD concentration were cultured alongside stage-matched groups with either similar amounts of 95% ethanol vehicle or without treatment. After 24 hours, conceptuses were fixed (4% PFA, 2 hours, 4°C), rinsed in PBS, and X-gal stained (Daane and Downs, 2011). Embryos treated with 20 μM KAAD, exhibited the fewest defects but the most residual *Ptch1* (data not shown). Embryos treated with 50 μM KAAD exhibited expected somite numbers and residual *Ptch1* in the posterior notochord (Fig. 5A, B). At higher KAAD concentrations, all embryos were significantly abnormal. For all subsequent experiments, embryos were cultured in the same lot of KAAD-cyclopamine, at 50 μM KAAD (+KAAD); controls were untreated embryos and those treated with the same ethanol vehicle used to make that particular batch of KAAD. No discernable differences were observed between vehicle-treated and untreated controls.

Three-dimensional (3D) reconstruction of histological sections

The Amira software system (Visualization Sciences Group, Burlington, MA) was used to create 3D reconstructions as previously described (Rodriguez et al., 2017). Briefly, sequential sectional images were loaded into Amira and made into an object with 3D voxel dimensions of 1x1x6 voxels (1 voxel = 1 μm) to volumize the 2D images by their 6 μm sectional thickness. The sections were then re-aligned in pairwise fashion and re-sampled. The structures within each section were then colored to correspond to each tissue in the resultant 3D reconstruction. After all sections were labeled, the surface generator compiled the snapshot views and computed a free-form surface model.

Measurements

The length of the AX as well as the proximal ACD (i.e. AX-associated ACD) was taken as the vertical distance from the amnion to the allantoic-yolk sac junction, while the length of the distal ACD (i.e. AX-liberated ACD) was taken as the vertical distance from the allantoic-yolk sac junction to the distal-most end of the allantois' Brachyury-positive core. The length of the visceral endoderm's high *Ptch1* domain, the dAX, was taken as the vertical distance of the darkest blue stained region of the visceral endoderm from the allantois-yolk sac junction, and enhanced by NIS Elements' "Look-Up Table" (LUT), which was used as an intensity thresholding tool to eliminate background pixel noise and bring out the regions of highest intensity from which the high *Ptch1* domain could be measured. Similarly, the distance of the CASPASE-3-positive border cell found at the distal limit of the high *Ptch1* dAX was taken as the length of the dAX from the allantois-yolk sac junction to the border cell.

Statistics

While no statistical method was used to predetermine sample size (n), for all experiments, $n \geq 3$ for all stages and all genotypes. Analyses for differences between group means were carried out via two-tailed Student t-Tests in Excel, while analyses for differences between observational frequencies were carried out via two-tailed Fisher's exact tests in GraphPad. *P*-values < 0.05 were considered statistically significant, and denoted by asterisk(s) in graphs. Chi-square analysis was used to determine Mendelian segregation ratios in littermates that involved the TTR-CRE transgenic mice.

RESULTS

Working hypothesis: the axially located allantois-associated extraembryonic visceral endoderm (AX) exfoliates mesoderm through contact with the primitive streak

In this study, our goal was to test the hypothesis that allantois-associated extraembryonic visceral endoderm (AX), which forms a single layer of epithelium adjacent to the allantois, is a bipotential mesendodermal tissue *in vivo*. Toward this end, we first synthesized previous key results to create a working model (Fig. 1A-C).

Prior to the allantoic bud stages, the streak achieves its posteriormost limit, entering the exocoelom and stopping just short of the prospective blood islands, where it positions the allantoic-yolk sac junction (Rodriguez et al., 2017) (not shown). The AX encompasses that

axial region in contact with the streak, and which expresses very little *Ptch1* (Daane and Downs, 2011), indicative of Hedgehog signaling (Goodrich et al., 1995). There is no high *Ptch1* domain at this time. A continuous basement membrane separates the primitive streak from the AX (Downs et al., 2009; Mikedis and Downs, 2009). During the neural plate/allantoic bud stages (~E7.25-7.5) (Fig. 1A), the basement membrane has broken down (Downs et al., 2009; Mikedis and Downs, 2009) and the allantoic bud appears (Fig. 1A).

By the headfold stages (Fig. 1B), the streak has matured into the allantoic core domain, or ACD, which is in contact with the AX (Downs et al., 2009). The AX continues to express low levels of *Ptch1* (Daane and Downs, 2011). The allantoic-yolk sac junction, a key feature of this model, advances toward the embryo (Rodriguez et al., 2017); the primitive streak, via *Brachyury*, organizes allantoic angioblasts here into the vessel of confluence (Rodriguez et al., 2017). At this point, allantoic mesoderm is now taking on its characteristic projectile shape (Rodriguez et al., 2017). Distal AX (dAX), as well as its associated yolk sac mesoderm and the ventral wall of the allantois, now inexplicably express relatively high levels of *Ptch1* (Daane and Downs, 2011). Smoothened, the signal transducer of the Hedgehog pathway (Chen et al., 2002), and its ligand, Sonic Hedgehog (SHH), are also found here (Daane and Downs, 2011). However, as immunohistochemistry was not as sensitive as *Ptch1* expression in resolving relative differences in levels of Hedgehog signaling (Daane and Downs, 2011), we favored use of the *Ptch1:lacZ* reporter mouse to ascertain relative levels of Hedgehog throughout this study (Materials and Methods).

During early somite stages (1-4s; ~E8.0-8.5) (Fig. 1C), the allantoic-yolk sac junction advances further anteriorly toward the embryo (Rodriguez et al., 2017); concomitantly, the AX shortens, while the dAX lengthens. Thereafter, the allantois, now a fingerlike projection, unites with the chorion (Downs, 2002; Downs and Gardner, 1995) (not shown). How the allantois becomes morphologically crafted into its sausage-like shape is not known.

To address this, and the role of the AX and primitive streak in building the fetal-placental interface, the following working model was proposed. First, as long as the AX is in contact with the primitive streak, *Ptch1* levels remain low and the AX exfoliates extraembryonic mesoderm. As AX-derived mesodermal cells enter the yolk sac and prospective allantoic bud, they separate the primitive streak from the AX, inducing high expression of *Ptch1* there. Increased Hedgehog signaling now liberates mesoderm from the AX, and creates the dAX domain which, due to its content of high *Ptch1*, ceases the EMT. This process of association and dissociation between exfoliating mesoderm and the AX, with concomitant refreshing of the allantoic-yolk sac junction by a new dAX, will be repeated down the length of the visceral endoderm, zipper-like, until the allantois is freed and shaped into its characteristic projectile.

DiI-labeling the AX tracks descendant cells into the fetal-placental interface

We defined the AX over time, establishing that its length decreased (Fig. 1D) concomitant with anterior advancement of the allantoic-yolk sac junction (Rodriguez et al., 2017). As ascertained by T-immunostaining transverse histological sections (Downs et al., 2009, Fig. 1I, J of that study), the width of the AX encompassed that part of the allantois that is in contact with the primitive streak. The AX was then labeled with DiI (Fig. 1E, F), a

fluorescent lipophilic dye that persists in the membrane of descendant cells over many generations (Krishnamurthy et al., 2008). It is used extensively to track cell movements and cell fate, which are essentially equivalent, as many cells are dividing as they translocate through the embryo in a variety of organisms, including the mouse (Beddington, 1994; Kinder et al., 1999; Sulik et al., 1994; Thomas and Beddington, 1996; Thomas et al., 1998) and chick (Selleck and Stern, 1991). Moreover, this classical method, which does not rely upon gene expression, provides an unbiased account of tissue lineage.

Preliminary results showed that, on average, application of DiI encompassed a cohort of ~304 ± 11.2 (SEM) AX cells (n=15; bud-2s stages) and never exceeded the width of the allantois (Fig. 1F). Confocal imaging immediately after labeling verified that DiI had not penetrated to the cells beneath it (Fig. 1G). Further, the AX was molecularly homogeneous for transthyretin (Fig. 1H), indicating that all labeled cells were visceral endoderm-like in nature (Mesnard et al., 2006).

After culture to 7-8s (~E8.5), when hindgut formation is underway and the major vasculatures have coalesced at the vessel of confluence (Downs et al., 1998; Rodriguez et al., 2017), DiI was found within cells of the yolk sac and allantois (Fig. 1I, J). Labeled cells located closest to the visceral endoderm were covered entirely with DiI (Fig. 1K), and overlapped Na^+-K^+ ATPase, found on all cell membranes (Fig. 1M); these observations showed that DiI labeled the plasma membrane, and suggested that DiI-rich cells were the most recent to emerge from the AX. Others, especially those farther away, exhibited DiI as spots on the cell membrane (Fig. 1L), consistent with those reported in other fate mapping studies (e.g., (Sulik et al., 1994)). This profile accords with high rates of allantoic proliferation during the bud-headfold stages (Downs and Bertler, 2000), resulting in dilution of DiI signal upon repeated cycles of replication (Krishnamurthy et al., 2008).

Proliferation in this region was verified with Ki67 (Gerdes et al., 1983) (Fig. 1N-Q). At bud stages, both the AX and allantois were proliferative throughout (Fig. 1N). By the headfold stages, the AX and immediately adjacent allantoic cells, which are part of the ACD, were proliferative compared to the rest of the ACD, which was relatively dormant (Fig. 1O, P). At 4s, as the hindgut forms and the ACD regresses toward the embryo (Downs et al., 2009), the allantois resumed global proliferation (4-6s stages) (Fig. 1Q).

AX contributes widely to the fetal-placental interface

DiI-labeled conceptuses were cultured to 6-10s stages (~E8.5-9.0), photobleached, and analyzed by histology to elucidate AX contribution to internal tissues. The tissues found at this time at the fetal-placental interface are summarized in Fig. 2A. The AX, continuous with the hindgut lip, or caudal intestinal portal and found at the entrance to the hindgut, ultimately becomes the hindgut lip (this study). The ventral wall of the allantois (“ventral cuboidal mesoderm”, VCM, (Daane et al., 2011)), which exhibits unique epithelial-like properties (Daane et al., 2011), extends toward the embryo to become splanchnic mesoderm (Daane and Downs, 2011), part of the primary body wall (Brewer and Williams, 2004). The yolk sac omphalomesenteric artery (OA), an axial blood vessel that becomes joined to the umbilical artery and fetal dorsal aortae at the vessel of confluence (Rodriguez et al., 2017), forms next to the hindgut.

Photobleached whole mount specimens confirmed that AX-derived cells ended up in the allantois and could be observed, to a first approximation, on its ventral wall after removing the yolk sac (Fig. 2B). In histological sections, background signal in unlabeled visceral endoderm was never completely abolished (Fig. 2C), despite long incubation times in hydrogen peroxide (Materials and Methods). Thus, the status of the AX could not be assessed after culture by the method of photobleaching. As described in a subsequent section, confocal microscopy, which eliminates the step of photoconversion into a solid precipitate, was used for this purpose. For now, only internal tissues, which were completely devoid of background (Fig. 2C), were evaluated by photobleaching.

At all stages, AX-derived cells contributed to hindgut endoderm (Fig. 2D, H) and to yolk sac mesothelium (Fig. 2E, H). However, contributions from early bud and headfold stage-labeled AX were predominantly to the allantois, including its ventral wall, primitive streak/ACD, umbilical artery and vessel of confluence (Fig. 2E, H). In addition, contribution was found in a rod-like structure (Fig. 2E, H), which we had previously observed extending from the ACD through the axial midline of the allantois (Downs et al., 2009) and which resembled here the bifurcation of Jurand (Jurand, 1974). Confocal imaging this structure in AX-labeled late bud stage conceptuses confirmed that it originated within the AX (Fig. 2G). At somite stages, while the AX continued to supply mesoderm to the major allantoic blood vessels, i.e., vessel of confluence and umbilical artery (Fig. 2H), the major recipients of AX-derived mesoderm were splanchnic mesoderm and the yolk sac omphalomesenteric artery (Fig. 2A, F, H).

Given that transthyretin (TTR) localizes to visceral endoderm, including the AX (Fig. 1H), we next undertook genetic lineage tracing via visceral endoderm-specific transthyretin-driven CRE recombinase (TTR-CRE; see Materials and Methods) (Kwon et al., 2008). After dissection and immunohistochemistry, which was more sensitive than imaging by fluorescent excitation (not shown), we examined the AX in at least three CRE-induced conceptuses per stage (neural plate/bud - 8s; 15 stages total separated by 2-4 hour intervals, >45 specimens), and compared results with similar numbers of *Ttr::Cre*$^{+/+}$ controls. In contrast to results of *in situ* DiI fate mapping, the only evidence that we could find during this timeperiod for GFP contribution to underlying extraembryonic mesoderm was unconvincing brown staining in some cells closest to the allantois (Fig. 2I). By 8s, GFP presented as mosaic immunostaining in the hindgut lip and definitive endodermal cells of the nascent hindgut (Fig. 2J). By contrast, the columnar visceral endoderm of the yolk sac, with which the hindgut lip is contiguous, exhibited uninterrupted and robust GFP (Fig. 2J). Examination of later-stage specimes (11-14s, ~E9.25; N=10), showed that, while darkly reactive GFP was present within yolk sac visceral endoderm and the hindgut (Fig. 2K), in accord with previous results (Kwon et al., 2008), a less intense GFP reaction was also found within extraembryonic mesoderm that was not found in a similar number of controls (Fig. 2K). However, given the non-specificity of the genetic lineage tracing method, we could not verify that contribution was specifically from the AX. Thus, while the AX might have delaminated extraembryonic mesoderm in the TTR-CRE inducible strain, we did not pursue this approach, as gene expression might be delayed and/or spurious in the extraembryonic mesoderm at later stages (see Discussion). It was doubtful that other reporter combinations would improve the signal, as contribution to extraembryonic mesoderm was not previously

noted (Kwon and Hadjantonakis, 2009; Kwon et al., 2008). Finally, the putative gene expression delays observed in this TTR-CRE recombinant mouse line argue against its utility in any future live imaging AX-derived cells when the AX was most active (Fig. 2H).

Next, to seek support for our hypothesis that contact with the primitive streak promoted AX mobilization into extraembryonic mesoderm, a segment of axial yolk sac blood island visceral endoderm, which was directly contiguous with the AX and not in contact with the primitive streak, was DiI-labeled. Yolk sac blood islands originate within the epiblast-derived primitive streak, which supplies them in two mesodermal waves (Kinder et al., 1999). In the dissection microscope, the blood islands are easily morphologically distinct from the AX as groups of blood cells located near the chorion. The visceral endoderm of the prospective blood islands was DiI-labeled in register with the AX, and thus, the axial primitive streak, at a variety of stages (OB, LB, EHF; n=9). Results showed that, after culture to 4s, when the blood islands are restricted to the circumferential yolk sac blood ring, only one labeled internal cell was found in each of two LB-stage labeled specimens (Fig. 2K-O). Moreover, PTCH1 and Indian Hedgehog (IHH), a major PTC ligand, co-localized only to the blood island visceral endoderm (Fig. 2K-O), consistent with a role for IHH signaling in induction of yolk sac blood islands (Dyer et al., 2001).

Based on results thus far, we preliminarily conclude that, as soon as the primitive streak extends into the exocoelom, the low *Ptch1* AX delaminates and, over time, sequentially contributes mesoderm first to the allantois, and then to the more mature fetal-placental interface. Contributions to the allantois included the allantoic core domain (ACD), hitherto assumed to be composed only of epiblast-derived tissue, consistent with it being part of the primitive streak (Downs et al., 2009). Also, contribution to the allantoic rod-like cells reinforced the possibility that Jurand bifurcations existed. Throughout this period, the AX also supplied the yolk sac and hindgut with mesoderm and endoderm, respectively. By contrast, axially located yolk sac blood island visceral endoderm did not contribute to underlying mesoderm as would have been expected if DiI contribution to the extraembryonic mesoderm were obtained by endocytosis and transfer to underlying cells, especially as extraembryonic visceral endoderm of the yolk sac exhibits far more vesicles than transitional visceral endoderm of the AX (Downs et al., 2009). Thus, the AX alone appeared to be a bipotential mesendodermal tissue.

AX undergoes an epithelial-to-mesenchymal transition (EMT)

Some histological specimens exhibited streams of photobleached cells entering the allantois from the AX as linear arrays (e.g., Fig. 3A). Closer morphological scrutiny showed whole cells appearing to leave the epithelium (Fig. 3B). Together with results of DiI fate mapping, these observations suggested that the AX uniquely undergoes an epithelial-to-mesenchymal transition (EMT).

To explore this possibility, we turned to confocal imaging, as immunostaining could be readily combined with DiI fate mapping. We further predicted that this method would be more sensitive than immunostaining to also allow us to detect gaps in the AX. We first asked how quickly DiI-labeled AX cells exited the epithelium. After 5 hours, and in accord with our preliminary observations (Fig. 1J-M), small numbers of whole cells, the membranes of

which were covered with DiI (Fig. 3C), had left the endoderm in the majority of specimens (n=8/13; 60%; bud-headfold stages). Zonula occludens-1 (ZO-1), which identifies epithelial tight junctions (Stevenson et al., 1986), localizes to visceral endoderm (Daane et al., 2011) and here was used to identify small gaps within the AX epithelium (Fig. 3D). An average of 29 gaps was quantified in the AX at a representative stage (early headfold, n=3). Each gap was roughly equivalent to one cell nucleus, and together, they encompassed ~37% of the total AX area (total area =6226.6±1121.5 (SEM) μm^2; ~77.2±6.1 (SEM) cells). The presence of cell-sized gaps reinforced morphological observations that entire cells were leaving the visceral endoderm. This was further supported by profiles of E-cadherin (E-CAD), a component of adherens junctions (Pokutta and Weis, 2007), which revealed loss of the junctional protein between neighboring AX cells (Fig. 3E).

As cells exited the AX, neighboring AX cells appeared to fill in the gaps, possibly by dividing, as mitotic profiles were often found within this tissue (e.g., Fig. 3F); this was consistent with the aforementioned proliferation profiles of the AX (Fig. 1N-Q). DiI-labeled visceral endoderm cells lateral to the AX, i.e., outside the bounds of the allantois, showed no movement toward the axial midline, and more importantly, no contribution to internal cells. Rather, they remained as a cohesive group within the lateral yolk sac endoderm (data not shown), highlighting differences between axial and non-axial regions of extraembryonic visceral endoderm. Thus, EMT activity is confined to the AX, which is in contact with the primitive streak.

The allantois of most amniotes is thought to contain an endodermal component (Mossman, 1937). Although we had previously searched for evidence of such an endodermal allantoic component in the mouse by morphology and immunohistochemistry, we failed to find it (Daane et al., 2011). This suggested that the molecular identity of AX cells changes as they transit from the visceral endoderm to extraembryonic mesoderm. FOXa2, which localizes to the nuclei of endoderm cells (Kubo et al., 2004), and is found in the AX (Wolfe et al., 2017), was present in DiI-labeled visceral endoderm cells that had not left the AX (Fig. 3G-J). However, during transit, AX-transitioning cells down-regulated FOXa2, which now appeared as small spots (Fig. 3H-J).

By contrast, the AX was relatively negative for N-cadherin (N-CAD), which is characteristic of many mesodermal cells (Hatta et al., 1987) (Fig. 3K). N-CAD-negative cells often appeared to be leaving the AX along its length and entering the allantois, which were, on the whole, N-CAD-positive (Fig. 3K). Monitoring the influx of labeled cells into the allantois by DiI formally demonstrated that, originally N-CAD-negative, AX derivatives acquired N-CAD upon completing their transition (Fig. 3L). Further, a timecourse of SNAIL (headfold-6s stages), which localizes to mesoderm in response to Hedgehog signaling (Li et al., 2006), revealed that, while the AX did not exhibit SNAIL, most allantoic cells immediately adjacent to it did (e.g., Fig. 3M). SNAIL was found throughout the allantois at all stages examined, but not all allantoic cells were positive (Fig. 3M, and data not shown). In addition to these molecular profiles, occasional round PECAM-1-positive hematopoietic-like cells were observed within the AX itself (Fig. 3N; n=2/6 specimens, 4s stage), consistent with *Runx1*'s presence there (Daane and Downs, 2011).

Together, these data provide evidence that visceral endoderm cells are transformed into mesoderm via an EMT. In the process, they lose ZO-1, E-CAD, and FOXa2 and acquire N-CAD and, possibly, SNAIL, properties consistent with an EMT (Shook and Keller, 2003). Moreover, PECAM1 and *Runx1* foretell hypoblast conversion into mesodermal hemogenic elements.

Contact with the primitive streak modulates expression of *Ptch1* in the AX, allowing exfoliation into extraembryonic mesoderm

Our working model predicted that signaling from the primitive streak regulates *Ptch1* in the AX, ensuring a low level of expression that permits the EMT (Fig. 1A). Then, as the AX becomes separated from the streak's allantoic core domain (ACD) by insertion of AX-derived extraembryonic mesoderm, the AX is no longer within range of those signals that emanate from the streak, and *Ptch1* becomes highly expressed to a level that releases AX-derived mesoderm (Fig. 1B). In the process, a new domain, the *Ptch1*-positive distal AX (dAX), is created that refreshes the allantoic-yolk sac junction, advancing it (anteriorly) toward the embryo. On that basis, the following parameters were predicted. First, the total length of the AX/dAX would be equivalent to the total length of the ACD, both its distal and proximal components. Second, exfoliation of AX-derived mesoderm would "push" the streak away from contact with the AX, thereby creating the dAX and de-repressing *Ptch1*. And finally, the high *Ptch1* domain would be longest in homozygous *T-curtailed* mutants compared to littermates as a result of a defective ACD failing to extend fully into the exocoelom.

Comparing the length of the low and high *Ptch1* domains and correlating these measurements with the length of the proximal and distal components of the ACD (Fig. 4A-D), we found that, as the low *Ptch1* AX domain shortened over time, the high *Ptch1* dAX domain lengthened (Fig. 4C). The proximal part of the ACD, which remained in contact with the AX, was similar in length to the low *Ptch1* AX domain, while the distal component of the ACD was similar in length to the high *Ptch1* dAX domain (Fig. 4C). Together, the length of the dAX and AX was equivalent to the length of the distal and proximal ACD, respectively. These measurements therefore supported our working model that the dAX and primitive streak had once been closely associated. This relationship could be readily visualized in histological sections (Fig. 4D).

The next prediction was that, as AX-derived mesodermal cells were added to underlying tissues, they separated the ACD from the AX. DiI-tracing the AX followed by T-immunostaining, which identified the ACD, showed the presence of T-negative cells between the AX and ACD/primitive streak (Fig. 4E-H).

Finally, we turned to analysis of *T-curtailed* mutants. Accordingly, the high *Ptch1* domain was shortest in the wildtype (Fig. 4I, L), intermediate in T^{+}/T^{C} heterozygotes (Fig. 4J, L), and longest in the T^{C}/T^{C} mutants where contact between the AX and streak was most abbreviated (Rodriguez et al., 2017) (Fig. 4K, L). This suggests that contact with the primitive streak represses *Ptch1*.

However, in the mutants, both $T^{C}/+$ and T^{C}/T^{C}, the high *Ptch1* domain was not limited to the dAX, i.e., that region distal to the allantoic-yolk sac junction (Fig. 4I-K, arrow); high *Ptch1* had spread into the AX. This may be due to a defective primitive streak/ACD. Specifically, through allantoic bud stages, the distal component of the streak morphologically breaks down, indicative of a defective posterior ACD (Rodriguez et al., 2017). Here, as a result of being able to visualize the mutant T protein during the same stages (Inman and Downs, 2006b), relative diminution of T was observed in the distal streak region of both heterozygotes and homozygotes (Fig. 4J, K) compared to wildtype (Fig. 4I). Thus, while the $T^{C}/+$ and T^{C}/T^{C} AX was in contact with the ACD, it was in contact with a defective streak, which was not able to de-repress *Ptch1*.

Finally, we note that the width of the high *Ptch1* domain, while expanded in the mutants, was not statistically different between $T^{C}/+$ and T^{C}/T^{C} (Fig. 4M). Thus, though it will not be explored here, the left-right axis of the high *Ptch*1 domain is not dependent upon the number of normal copies of *T* present, while its antero-posterior extension is.

Together with our findings that that AX, which is the only segment of extraembryonic visceral endoderm in contact with the primitive streak and which undergoes exfoliation (previous section), we tentatively conclude from these results that the primitive streak modulates *Ptch1*.

High Hedgehog liberates AX-derived mesoderm, thereby crafting the signature allantoic projectile

On the basis of the aforementioned observations, Hedgehog signaling might be involved in the visceral endoderm's EMT. To investigate this, a pharmacological approach was used to inhibit Hedgehog signaling, as application of the inhibitor and its outcome could be closely monitored at specific developmental timepoints. 50μM KAAD cyclopamine (KAAD) globally reduced *Ptch1* expression at a gross level in the inhibited specimens, with some expression persisting in the posterior embryonic notochord (Fig. 5A, B; Materials and Methods); chorio-allantoic union was not affected. After four hours of treatment, *Ptch1* was significantly reduced in the dAX, resulting in the loss of the high *Ptch1* domain (Fig. 5C, D). Residual *Ptch1* expression in associated yolk sac mesoderm was not unexpected, as this tissue was not in direct contact with the culture medium.

The dAX was sometimes multilayered after inhibition (n=6/13, LB-EHF stages; Fig. 5D). We therefore asked whether the AX had been transformed into another cell type in the presence of KAAD. The most obvious candidate was parietal endoderm because upon inhibition with the Hedgehog antagonists, cAMP and forskolin, visceral endoderm of embryoid bodies differentiates into parietal endoderm (Maye et al., 2000). Neither untreated nor KAAD-treated AX exhibited SNAIL (data not shown), which identifies parietal endoderm (Fig. 3L) (Kunath et al., 2005). Thus, to a first approximation, AX identity was not changed by loss of Hedgehog. Multilayering of the AX might therefore represent failure of cells that were actively transitioning into mesoderm at the time of KAAD application to become liberated from the AX. This was investigated by DiI fate mapping, below.

We compared the status of PTCH1 and SHH in DiI-labeled untreated (Fig. 5E-I) and KAAD-treated conceptuses (Fig. 5J-N). In untreated specimens, many labeled cells had clearly departed the AX, i.e., were “liberated”, and no longer exhibited SHH (Fig. 5I); those AX-derived mesodermal cells that had not left the epithelium but remained juxtaposed to, or associated with, the AX exhibited both SHH and PTCH1 (Fig. 5N). By contrast, KAAD-treated AX-derived cells seemed to remain associated with the AX, with fewer cells being liberated (Fig. 5N); most of these were negative for PTCH1 and SHH, confirming that KAAD inhibition was successful.

Quantification of the total number of AX-derived mesodermal cells associated with the AX in bore this out (Fig. 5O). While the number of fully liberated AX-derived cells was significantly reduced in +KAAD, the number of AX-derived cells that were ingressing but in contact with the AX was similar in both ±KAAD. Moreover, by adding the status of PTCH1 and SHH to each plot, we observed that, to be fully liberated, the AX-derived mesodermal cells must drop SHH.

While the allantoic-yolk sac junction had, as expected, shifted proximally toward the embryo in controls (Fig. 5P, Q, S), it appeared stuck in the treated specimens, resulting in failure to refresh and re-position the allantoic-yolk sac junction upon resolution of the EMT (Fig. 5P, R, T). The frequency of abnormal attachments between the allantois and yolk sac, as determined by placement of the allantoic-yolk sac junction, was highest when KAAD was applied at the pre-bud neural plate (“OB”) stage, when the EMT commenced, and decreased when KAAD was added at later stages (Fig. 5U). T localization was unchanged in the KAAD-treated specimens (Fig. 5S, T). Thus, low levels of Hedgehog permit exfoliation of the AX, enlarging the latter’s domain, while high levels of Hedgehog signaling resolve it, leading to fully liberated AX-derived mesodermal cells. On the basis of these observations, we conclude that Hedgehog, via modulation of the EMT, crafts the allantoic projectile.

Hedgehog signaling individualizes the posterior arterial blood vessels

The allantoic projectile does not form in the absence of Hedgehog. We therefore investigated the consequence of Hedgehog inhibition on the mature fetal-placental interface, especially the relationship between the prospective omphalomesenteric artery and visceral endoderm (Fig. 6A-C), the vessel of confluence (VOC) and yolk sac (Fig. 6A, D, E), and the status of the umbilical artery (Fig. 6A, F, G).

Inhibition at the pre-bud (“OB”) stage resulted in a collection of small blood vessels that failed to articulate into a single arterial vessel (Fig. 6A-C). The VOC which should have been a detached vessel surrounded by splanchnic mesoderm (Fig. 6A, D), was stuck to the yolk sac, and splanchnic mesoderm of the primary fetal body wall was a disorganized mass (Fig. 6E). The umbilical artery, which should have been a free and distinct vessel, and not associated with the hindgut (Fig. 6A, F), was stuck to the yolk sac, and associated with an abnormally positioned hindgut in the embryonic tail (Fig. 6A, G).

Three-dimensional reconstruction of specimens which had been inhibited at slightly later initial stages (EHF-1s) and cultured longer (9-13s) revealed fewer abnormal attachments to the visceral endoderm; the majority exhibited an individualized VOC and umbilical artery

(Fig. 6H, I), probably because the allantoic projectile had been partially resolved from the visceral endoderm at the time of KAAD application. However, those prospective vessels destined to coalesce into the omphalomesenteric artery failed to do so, instead making abnormal lateral attachments to the dorsal aortae (Fig. 6H, I). By 12-13s, when the embryo is turning and the VOC recurves over the hindgut to form the medial umbilical roots (Rodriguez et al., 2017), the VOC failed to form these roots, and the posterior region was largely stunted in development (Fig. 6J, K). These later-stage inhibition data show that Hedgehog signaling is required to individualize the posterior arterial system of the placentae. They also corroborate results of fate mapping (Fig. 2H) which show that by the headfold-1s stages, most of the allantois has already been built, and therefore, is largely unaffected by KAAD inhibition. However, contribution to the VOC, a fixed point at the allantoic-yolk sac junction, continued to expand at later stages to ensure the formation of the medial umbilical roots, which transiently mark the site of formation of the lateral umbilical roots that eventually lead to vascularization of the hindlimbs (Gest and Carron, 2003).

The AX becomes the hindgut lip, the next-phase source of mesendoderm that builds the fetal-placental interface

As described in a previous section, the fate of the AX could not be tracked by photobleaching (Fig. 2C). Thus, confocal imaging was used. When labeled at the bud stages (~E7.25-E7.5) and briefly cultured to 2s, the AX cell surface was still relatively solidly labeled (Fig. 7A-C). When examined at the onset of hindgut formation (4-7s), only the dAX exhibited high levels of DiI (Fig. 7D-F). The dAX had therefore ceased undergoing the EMT, corroborated by its remaining solidly *Ptch1*-positive (Fig. 6A). By contrast, the AX, which had become the hindgut lip, exhibited spotty DiI (Fig. 7D-F), and relatively low *Ptch1* expression (Fig. 6A), suggesting that, as the former AX, it might be undergoing an EMT.

To test this, the dAX was labeled (n=3, LB stage) and conceptuses were cultured to 6s. The dAX delaminated mesoderm, but contribution was superficial, involving only the yolk sac mesoderm and ventral allantoic wall; internal allantoic structures were negative (data not shown). These limited contributions indicated that, as the AX separated from the streak to become the dAX, high *Ptch1* levels caused the EMT to slow down.

To investigate its fate, the hindgut lip (Fig. 7G) was DiI-labeled (5-9s stages) (Fig. 7H). Immediate inspection verified that DiI was limited to the hindgut lip and did not penetrate to underlying tissues (Fig. 7I, J; n=7). After 20 hours in culture, whole mount analysis showed that hindgut lip-derived labeled cells ended up along the embryonic midline, from the tip of the tail to the open hindgut at all stages (Fig. 7K; n=7). As tissue thickness at older stages precluded adequate photobleaching and analysis of the full spectrum of interior tissue contributions, we cultured labeled embryos for half the time (~10-12 hours), followed by photobleaching and analysis. At all stages, the hindgut lip contributed to the dorsal, lateral and ventral components of the hindgut, associated somatopleure, the omphalomesenteric artery and associated splanchnopleure, fetal dorsal aortae, posterior loose embryonic mesoderm and, if the final stage was > 9s (n=4/6) the embryonic notochord (Fig. 7M, N). The allantois never exhibited label (Fig. 7N). The corresponding tissues in unlabeled controls were completely negative (Fig. 7O, P).

We conclude that the AX becomes transformed into the hindgut lip, forming the next-phase posterior mesendodermal cell pool and contributing to both embryonic and extraembryonic tissues at the fetal-placental interface. At the same time, high levels of *Ptch1* in the dAX result in cessation of the EMT and retention of DiI.

A single cell, whose identity is regulated by Hedgehog signaling, is located between the distal AX and non-EMT blood island visceral endoderm

The AX and visceral endoderm of the yolk sac blood islands form an axial continuum. Yet, only the AX underwent an EMT. To find out whether some sort of special feature might separate these two domains, we examined the axial visceral endoderm along its full length, from the level of the amnion to the level of the chorion. During early bud-headfold stages, multiple breaks were observed in the AX of most specimens (Fig. 8A), consistent with results of ZO-1 immunostaining (Fig. 3D). None of these breaks was associated with CASP3 (data not shown), and thus, associated cells were unlikely undergoing cell death (Köhler et al., 2002). However, at the early headfold-6s stages, a single axially placed CASP3-positive cell (Fig. 8B-D) was invariably sighted at the distal boundary of the dAX, separating it from the adjacent yolk sac blood islands in the majority of specimens (n=26/40; Fig. 8E, F). This CASP3 border cell did not appear to be undergoing apoptosis, as evidenced by comparison with trypan blue live cell exclusion (Fig. 8G). While we could not, for technical reasons, co-localize CASP3 and trypan blue, a single trypan blue cell was located at the same distance as the CASP3 cells in only 3 of 21 specimens examined between the EHF and 5s stages (3/21 trypan blue cells versus 25/38 CASP3 cells, EHF-5s, two-tailed Fisher's exact test; P=0.0003). Given that morphological cell death is estimated to take 2-4 hours (Cordeiro et al., 2004), and that the timeperiod between each developmental stage in this study is ~2-4 hours (Downs and Davies, 1993), CASP3 is therefore unlikely associated with cell death. After 4-9 h of KAAD treatment, the site-specific CASP3 cell was absent in the majority (96.9%) of specimens (initial/final stages: OB-1s/EHF-2s) (Fig. 8H-J), suggesting that the unique CASP3 border cell is regulated by Hedgehog. Putting these data together with the KAAD inhibition experiments (Fig. 5), loss of the CASP3 border cell correlated with expansion of the AX domain (Fig. 5Q-T, summarized in Fig. 8K, L).

The AX and primitive streak form a self-organizing center for the fetal-placental interface

We had previously shown that a midline file of cells was deposited in the wake of ACD retraction toward the hindgut (Fig. 9D of (Downs et al., 2009)). Based on its alignment with the antero-posterior axis, and similarities to the notochord, which emanates from the ventral node (Beddington, 1994) to provide structural support during trunk elongation (Lee and Anderson, 2008), we have referred here to this extension as an allantoic rod. As previously shown by synchronous orthotopic ACD grafts, this extension creates an axial cell file (Fig. 10C of (Downs et al., 2009)); a similarly grafted whole mount specimen is presented here for ease of visualization (Fig. 9A).

At early somite stages, removal of the ACD had resulted in remnant allantoises that failed to elongate to the chorion (Downs et al., 2009). Given that the AX contributes to both the ACD and the allantoic rod, we asked whether the AX was involved in allantoic elongation. For this, the ACD alone or the ACD+AX (LHF-2s stages) were heterotopically grafted into host

embryos (Fig. 9B), as this method of grafting, either synchronously (same stage) or asynchronously (different stages), can define the developmental potential of the donor tissue.

In the absence of the AX, grafted ACD's rounded up and formed non-polarized spheres (n=3/3) (Fig. 9B, C) which, by FOXa2 analysis, revealed no signs of hindgut endoderm, part of which is derived from the ACD (Mikedis and Downs, 2012) (Fig. 9D). In addition, a dense allantoic core was absent from these spheres. Instead, the spheres were filled with a disorganized vascular network. All but one of the spheres was free-floating; in that single tethered specimen, lateral visceral endoderm of the host and the donor ACD were in contact over an area (~7527 μm^2, or ~75 cells) equivalent to the size of the delaminating AX (Fig. 3D, 9D) which, based on results below, should have been sufficient to promote ACD elongation.

By contrast, the donor ACD+AX elongated into truncheon-shaped structures (Fig. 9B, E), one end of which was dense while the other was more expanded (n=4/4). Histological analysis revealed that, regardless of whether ACD+AX grafts had integrated into the host yolk sac (Fig. 9F) or were free-floating in the amniotic cavity (Fig. 9G), they formed antero-posterior polarized "stem-and-lollipop" structures that looked remarkably similar to the allantois and its associated hindgut *in vivo* (Fig. 9H). At the putative distal (posterior) end, loosely organized blood vessels were the only structural feature (Fig. 9F, G), similar to the intact allantois (Fig. 9H). At the other, proximal (anterior) end, cells were densely packed, with signs of tubule formation (Fig. 9F, G), similar to the intact allantois and associated embryonic hindgut (Fig. 9H).

FOXa2 immunostaining revealed a single proximal tube-like structure of the elongated complex (Fig. 9I, J) that was continuous with the donor AX (Fig. 9K), the latter of which rounded up and formed a cyst. The hindgut tubule and AX were associated with a large vessel (Fig. 9J, K) that we took to be the VOC and/or the omphalomesenteric artery (Fig. 2A, 9H). A single vessel extended through the proximal midline of the graft (Fig. 9I) which, because of its axial placement, we interpreted as the umbilical artery (Rodriguez et al., 2017). Associated with the hindgut tube were rosettes of cells unreactive for FOXa2 (Fig. 9I); as rosettes may be indicative of the presence of pluripotent cells (Edwards et al., 1970; Elkabetz et al., 2008; Zhang, 2006), we interpreted them, especially based on their proximal (anterior) position within the truncheon, to be components of the pluripotent ACD (Mikedis and Downs, 2012). When serendipitously oriented in a perfectly planar position, the rod-like allantoic extension was observed down the midline of the truncheon (Fig. 9L). Three-dimensional modeling showed that the rod was distinct from the PECAM1 umbilical artery (Fig. 9M).

To complete this analysis, we orthotopically and synchronously grafted the AX alone. Orthotopic synchronous grafts provide information about the approximate fate of a given tissue (Beddington, 1981), and were thus predicted to independently support results of DiI fate mapping. First, we verified that, after brief enzymatic treatment (Materials and Methods), the AX was devoid of associated cells (n=6/6; Fig. 9N). When orthotopically placed into bud-headfold stage conceptuses (n=6/6), the appropriate region of which represents a very small target site, the donor AX had a tendency to roll up, as described in

previous studies of grafted embryonic visceral endoderm (Copp et al., 1986). While the AX failed to incorporate into the host, nevertheless, after culture, unincorporated AX exhibited modest formation of mesoderm (Fig. 9O), as well as blood cell formation (Fig. 9P). Transformation of AX into blood cells further supported the idea that PECAM1 (Fig. 3N) and *Runx1* (Daane and Downs, 2011) within the AX, do, in fact, preview AX conversion into hemogenic elements of blood vessels. Thus, in the absence of contact from the streak, the AX undergoes a very limited EMT.

When later stage AX was synchronously orthotopically grafted into a larger allantois, and in contact with the host ACD, a larger structure than the bud-stage primitive streak (n=3/3), descendants of grafted AX cells contributed to the host's ventral hindgut, and a vast array of extraembryonic mesoderm of the omphalomesenteric artery, splanchnic mesoderm and allantois (Fig. 9Q), in accord with results of DiI fate mapping (Fig 2H). One of the chimeras, cultured to the time when the posterior arterial vessels undergo remodeling (Rodriguez et al., 2017), showed that the AX contributed to the medial umbilical roots (Fig. 9Q). The medial umbilical roots position the lateral umbilical roots; in turn, these become the common iliac arteries that divide the flow of blood from the aorta to the hindlimbs (Rodriguez et al., 2017).

Together, the AX+ACD self-organizes into the fetal-placental interface. In the absence of the AX, the ACD fails to exhibit A-P polarity and elongate, and the ACD cannot fulfill its potential to form endoderm. Thus, the AX imparts antero-posterior polarity to the ACD and its ability to elongate, as well as the potential to make definitive endoderm.

The allantoic rod is identifiable by Collagen Type IV

Finally, results of previous studies revealed a number of proteins present within cells of the allantoic midline. These included OCT-3/4 (Downs, 2008), STELLA (Mikedis and Downs, 2012; Wolfe et al., 2017), PECAM1 (Inman and Downs, 2006b; Naiche and Papaioannou, 2003) and Collagen Type IV (COLIV) (Mikedis and Downs, 2009). Self-organizing AX/ACD tissue combinations, above, showed that the allantoic rod is distinct from the PECAM1 umbilical artery (Fig. 9M); whether any other axially-located proteins might distinguish the allantoic rod from the nascent umbilical artery was not known.

To address this, COLIV was examined in archived material (Mikedis and Downs, 2009) at 5-6s, when the rod is first observable (Downs et al., 2009). COLIV, a major component of basement membranes which plays important roles in cell adhesion, migration, differentiation and growth (Aumailley and Timpl, 1986), was continuous between the visceral endoderm and the axial allantoic midline (Fig. 10A). All other specimens (Mikedis and Downs, 2009) exhibited similar but discontinuous COLIV profiles within the allantois due to imperfect sagittal orientation.

Three-dimensional modeling showed that the COLIV-rich allantoic rod emanated from the similarly COLIV-rich ACD (Fig. 10B), and extended through the allantoic midline (Fig. 10B). Like the T-positive embryonic notochord (Wilkinson et al., 1990) (Fig. 10C-E), which extends the body axis further anteriorly from its site of origin within the node (Beddington, 1994), the allantoic rod reached posteriorly, here, toward the chorion, and also exhibited T

(Fig. 10F-I); it was distinct from the PECAM1 axial file (Fig. 10J-M). DiI-labeled AX derivative cells co-localized COLIV (Fig. 10N-Q). Thus, on the basis of these results, we conclude that the allantoic rod is derived from the AX and is identifiable by COLIV.

Two normal copies of *T* are required for allantoic elongation to the chorion (Inman and Downs, 2006b) as well as for full streak extension into the exocoelom (Rodriguez et al., 2017). Both T^{+}/T^{+} wildtype and T^{C}/T^{+} heterozygotes exhibit elongated allantoises that fuse with the chorion (Inman and Downs, 2006b); by contrast, T^{C}/T^{C} homozygous mutants exhibit an allantois that fails to elongate (Inman and Downs, 2006b). We therefore queried the status of the allantoic rod in *T*-curtailed (T^{C}) littermates, asking whether loss of elongation in mutant allantoises might coincide with loss of the rod.

T^{+}/T^{+} wildtype and T^{C}/T^{+} heterozygotes exhibited the COLIV-defined allantoic rod, which was distinct from the PECAM1 umbilical artery (Fig. 11A-J, and data not shown; T^{+}/T^{+} n=4, T^{C}/T^{+} n=9). In accord with previous results (Rodriguez et al., 2017), PECAM1-positive angioblasts were disorganized in T^{C}/T^{C} homozygous mutants (Fig. 11K-T; n=3). While similarly disorganized clusters of COLIV were observed throughout the truncated T^{C}/T^{C} allantoises (Fig. 11K-T), the COLIV-positive rod was missing (Fig. 11K-T). No AX contribution to the T^{C}/T^{C} mutant allantois was observed. Thus, the T^{C}/T^{C} mutant AX failed to deliver mesoderm to the allantois and failed to create the allantoic rod. These data could be interpreted in two ways. First, they support the hypothesis that contact with some requisite length of the primitive streak is required for mobilization of the AX. Loss of full contact results in *Ptch1* de-repression, with failure of the EMT to progress. Alternatively, the T^{C}/T^{C} mutant AX did manufacture the rod, but it might have undergone apoptosis and was no longer detectable by the end stage here of 4s. This would accord with our previous observation that the allantoic midline of T^{C}/T^{C} mutants undergoes apoptosis by 2s, while wildtype and heterozygous littermates were generally unaffected (Inman and Downs, 2006b). Whatever the explanation, these observations suggest that the allantoic rod is required for allantoic elongation and, possibly, patterning allantoic angioblasts into the umbilical artery. Finally, the presence of allantoic mesoderm in T^{C}/T^{C} mutants accords with a previous study which showed that the T^{C}/T^{C} mutant allantois is derived, at least in part, from the embryonic posterior primitive streak (Inman and Downs, 2006b).

DISCUSSION

Contact between hypoblast/visceral endoderm and the primitive streak is one of the most enduring relationships in amniote development (Eyal-Giladi, 1970; Kwon et al., 2008). However, its significance is not well understood. On the basis of results here, we conclude that a small segment of visceral endoderm, the AX, and the primitive streak, or ACD, mutually interact between the bud and 4s stages to create the fetal-placental interface. We propose that contact with the primitive streak unleashes the AX's binary mesendodermal potential, inhibiting *Ptch1* expression there to allow exfoliation of mesoderm into the yolk sac and presumptive allantois. Mesoderm liberation from the AX is the result of loss of contact between the AX and the primitive streak, which results in de-repression of *Ptch1* and resolution of the EMT. By contrast, the AX imparts antero-posterior polarity on the primitive

streak/ACD, the streak's ability to elongate through the allantoic midline, and its potential to form embryonic endoderm.

We have previously reported the presence of T in both the ACD and AX (Downs et al., 2009; Inman and Downs, 2006a). However, we believe that the primitive streak, rather than cell autonomous T, modulates *Ptch1* in the visceral endoderm for the following reasons. First, of all extraembryonic visceral endoderm, only the AX is in contact with the primitive streak. The yolk sac blood island and lateral yolk sac visceral endoderm, which were devoid of such contact but exhibit T, albeit a cytoplasmic rather than nuclear version (Inman and Downs, 2006a), showed no signs of an EMT (Fig. 2L-P and corresponding text). Second, during the neural plate stages (OB, EB, and LB; ~E7.0-E7.5), when the entire length of the streak is juxtaposed to the AX (Downs et al., 2009; Rodriguez et al., 2017), levels of *Ptch1* in the AX are low, the EMT is underway (Fig. 2H), and T is not observed in the AX (Inman and Downs, 2006; Downs et al., 2009, Fig. 3C). Thus, T does not seem to be involved in regulating *Ptch1* in a cell autonomous manner. By the headfold stage, when T does appear in the AX (Inman and Downs, 2006; Downs et al., 2009), the average number of T-positive AX cells, ~23 (Downs et al., 2009, Fig. 3C of that study), divided by the average number of AX cells calculated in this study (304, bud-2s stages; Fig. 1F and text), represents only 7.6% of the total AX population. During this time, ~36% of AX cells were undergoing an EMT (Fig. 3D, and text). Even the highest absolute number of T-positive cells found in the AX (~70, 4s-stage, Downs et al., 2009, Fig. 3C), represents only 23% of the total number of AX cells. Thus, if T were involved in regulating *Ptch1*, we would have expected more T-positive cells in the AX and a mosaic of high/low *Ptch1* expression there; this was not observed. Fourth, grafts of the AX did not produce substantial mesoderm when not in contact with the AX (Fig. 9N-R). However, in future experiments, it would be informative to carry out AX grafts in the *Ptch1* reporter strain, and investigate levels of *Ptch1* in these after culture to find out whether it is high in donor AX that is no longer associated with the streak. Finally, while many studies have implicated T in the EMT in various cell lines (e.g., (Hamilton et al., 2012), results of studies *in vivo* favor an essential role for T in specification of cell fate, and not the EMT or cell proliferation (Zhu et al., 2016). Our data accord with a general role for T in stem cell identity within the AX, where it is found with other stem cell factors. These include OCT-3/4 (Downs, 2008; Wolfe et al., 2017), STELLA (DPPA3) (Mikedis and Downs, 2012; Wolfe et al., 2017), PRDM1 (BLIMP1) (MIkedis and Downs, 2017), MIXL1 (Wolfe and Downs, 2014; Wolfe et al., 2017) and FOXa2 (Wolfe et al., 2017). All of these persist within the AX through its transformation into the hindgut lip.

Model for genesis of the fetal-placental interface through interaction between the AX and the primitive streak

Figure 12 presents a model that illustrates the stepwise interaction between the AX and primitive streak in building the fetal-placental interface. In the first step, the streak has extended into the exocoelom (bud stage; (Downs et al., 2009; Rodriguez et al., 2017); Fig. 12A). Contact with the streak keeps levels of *Ptch1* low in the AX (summarized in Fig. 1A). Consequently, the AX exfoliates mesoderm to the visceral yolk sac and allantoic bud. Delaminating AX cells lose ZO-1 and E-CAD (Figs 3D, E), consistent with a classical EMT (Gonzalez and Medici, 2015). Exfoliation produces small cell-sized holes in the epithelium

(Fig. 3D, G-J). Intriguingly, holes in extraembryonic visceral endoderm had been anecdotally reported during mouse gastrulation (Kaufman, 1992), but their possible significance has been obscure. The gaps created by the exiting cells appeared to be filled in from nearby visceral endoderm, possibly through mitosis (Fig. 3F). Mitosis in the AX may have been triggered by a “stretching” mechanism, in which nearby cells temporarily fill in the small holes (Gudipaty et al., 2017); thereafter, proper cell number within the epithelium would have been restored through cell division. Exfoliation and mitosis of the AX can account for the streak’s expansion in primitive streak/ACD explants in previous experiments, which occurred only in the presence of the AX (Downs et al., 2009).

By the headfold stage, low and high levels of *Ptch1* were now apparent in the axial AX region, the associated yolk sac mesoderm, and the proximal ventral wall of the allantois (summarized in Fig. 1; Fig. 12B). As in the previous stages, low levels of *Ptch1* persist in the AX because this tissue is still in contact with the streak (Downs et al., 2009; Rodriguez et al., 2017); Fig. 12B1). Now, exfoliated mesoderm inserts itself between the AX and ACD, creating a new domain, the dAX, in which *Ptch1* is de-repressed and levels become relatively high (summarized in Fig. 1B; Fig. 12B2, 12B3). Because the lengths of the AX and dAX add up to the full length of the ACD (Fig. 4C), we conclude that the dAX was once physically in contact with the streak. Thus, from these observations, and arguments put forth in the previous section, we believe that the streak modulates *Ptch1*. This conclusion was further supported in T^C mutants, whose *Ptch1* domain expanded dependent upon the extent to which the streak contacted visceral endoderm (Fig. 4J, K), as well as by isolated grafts of the AX (Fig. 9O, P).

As shown by DiI labeling in the presence of KAAD (Fig. 5E-O, Q, R), high levels of *Ptch1* were required to release AX-derived mesoderm to the yolk sac and allantois. At the first signs of EMT resolution, a unique axial border cell appeared, identifiable by CASP3, which delineated high *Ptch1*-expressing dAX from the yolk sac blood islands (Fig. 8E, F; 12B3); the latter were not in contact with the streak, and consequently, did not undergo an EMT (Fig. 2L-P). Because morphological apoptosis and CASP3 were found in an overlapping site in just a small number of specimens (Fig. 8G), the role of CASP3 does not seem to be in destruction but rather in separation and possibly stabilization of the AX domain from the blood islands, consistent with CASP3’s roles in non-apoptotic processes (Fernando et al., 2005; Fernando et al., 2002; Huh et al., 2004; Li et al., 2010; Miura, 2012; Perez-Garijo et al., 2004) and linked to Hedgehog.

As the allantois completes elongation (Fig. 12C), the AX shifts its major contributions to nascent splanchnic mesoderm and the nascent omphalomesenteric artery. At the same time, the AX-derived allantoic rod becomes apparent (Fig. 2E, G; 10N-Q; 11A-J), and traverses the allantoic midline, suggesting that Jurand bifurcations do exist. This is not surprising as, in humans, the yolk sac-derived diverticulum forms the framework upon which the umbilical cord is built, and is distinct from the vasculature (George, 1942). Similarly, in the mouse gastrula, the allantoic rod runs parallel to and is distinct from the umbilical artery (Fig. 9M). The rod-like structure is missing in T^C/T^C mutants (Fig. 11), which fail to elongate (Inman and Downs, 2006b), and organize the umbilical artery (Rodriguez et al., 2017). In this way, the allantoic rod may thread its way into the ACD (Rodriguez et al., 2017), and with it,

organize the umbilical vasculature in mice. Thus, as previously suggested (Downs, 2009), the primitive streak appears to be capped at both ends by node and notochord/rod-like structures that extend the body axis in anterior and posterior directions in the embryonic and extraembryonic regions of the conceptus, respectively, thereby promoting the reach of the streak's organizational abilities around the midline.

By 7-10s, the allantoic-yolk sac junction is replaced by the high *Ptch1* dAX domain and splanchnic mesoderm (Fig. 12D). The AX, perhaps through passive morphogenetic translocation, becomes the hindgut lip, nearly exhausted of its original DiI-labeled cell population. The low *Ptch1*-expressing hindgut lip steps in as the next-phase mesendodermal cell reservoir and continues to build the fetal-placental interface, contributing to all mesendoderm-derived tissues in this region, both embryonic and extraembryonic. This was not surprising, as both the AX and hindgut lip are rich in a battery of proteins involved in stem cell biology and mesendodermal identity. In addition to OCT-3/4, STELLA, and PRDM1 (Mikedis and Downs, 2017), described in the previous section, MIXL1 (Wolfe and Downs, 2014), FOXa2 ((Wolfe et al., 2017) and this study), and RUNX1 (Daane and Downs, 2011; Wolfe et al., 2017) were found here. No other region of posterior extraembryonic visceral endoderm exhibits these and thus, they likely play roles in AX/hindgut lip potency and mesendodermal identity.

Intriguingly, hindgut endoderm itself is rich in *Ptch1* expression (Daane and Downs, 2011) and robust SHH is also found in the developing hindgut of human conceptuses (Odent et al., 1999). This suggests a conserved mechanism for hypoblast/visceral endoderm-mediated gut formation in both rodents and humans. However, the relationship between low and high *Ptch1* domains in this region remains unknown. As the hindgut lip is no longer in contact with the primitive streak beyond 6s (Downs et al., 2009, Fig. 4 of that study), future studies should be directed toward identifying those factors produced by the streak that promote the AX's EMT, as they may now be found in this region. In both scenarios, PERLECAN could be an important candidate, as PERLECAN regulates Hedgehog in *Drosophila* (Park et al., 2003) and is found at the AX/streak interface (Mikedis and Downs, 2009).

Thus, fate mapping experiments combined with protein localization and pharmacological inhibition produced a logical and internally consistent story concerning genesis of the fetal-placental connection. While we tried to support our results with genetic lineage tracing, the results were inconclusive. Visceral endoderm at large had previously been shown by genetic lineage tracing to contribute only to definitive gut endoderm (Kwon et al., 2008), which we validated and extended by showing that the AX in particular contributes to gut endoderm of the fetus. In accord with previous studies (Kwon et al., 2008), we found no evidence for contribution to mesoderm during the AX's optimal period of activity, i.e., neural plate - early somite stages. Given that the allantois is composed in large part of hematopoietic mesoderm (Corbel et al., 2007; Daane et al., 2011; Daane and Downs, 2011; Naiche et al., 2011; Zeigler et al., 2006), which may be the first to transit from the AX (Figs 3N, 9P), perhaps exfoliating TTR-CRE-induced cells died during the early EMT. Widespread developmental defects and apoptosis have been reported in CRE-inducible lines, especially in hematopoietic lineages (Naiche and Papaioannou, 2007). Alternatively,

immunofluorescence, the sole readout used in the previous study (Kwon et al., 2008), was not as sensitive as GFP immunonistochemistry (this study, and (Mikedis and Downs, 2017).

By 11s, TTR-CRE-induced reporter signal was observed in posterior mesoderm, though it was weaker than that found in the gut endoderm (Fig. 2J). It is tempting to conclude that use of genetic lineage tracing supported results obtained by classical fate mapping, but with the following caveats. First, mesoderm expression was delayed by more than two days from the time that contribution was first seen by *in situ* labeling at ~E7.0. While delays in gene expression are not unusual in CRE-inducible mouse lines (Mikedis and Downs, 2017), CRE mis-expression can equally explain the data. For example, segregation of the $Ttr::Cre^{Tg/+}$ allele did not follow expected Mendelian ratios (Materials and Methods), and thus it is possible that appropriate tissue-specific induction was affected as well, as noted with another CRE-inducible line (Mikedis and Downs, 2017). Also, mosaicism, previously anecdotally reported in the TTR-CRE inducible strain (Kwon and Hadjantonakis, 2009), was observed here in the AX/hindgut lip while the extraembryonic visceral endoderm of the yolk sac remained robustly and continuously positive (Fig. 2J). Mosaicism in inducible mouse lines has previously been explained by intercalation of non-transgenic neighboring cells (McCann et al., 2012). In light of these caveats, we suggest that future studies using CRE-inducible mouse lines employ, as we have here, multiple fate-mapping approaches.

Fig. 12E presents a revised fate map of the mouse zygote through early gastrulation (adapted from (Gardner, 1983)), incorporating and building upon results of the previous study which showed that visceral endoderm contributes to definitive gut endoderm (Kwon et al., 2008). Topographical differences exist between the mouse and human gastrula (Fig. 12F, G), with the human forming a flat disc (Fig. 12F) and the mouse forming an inverted U-shape (Fig. 12G). Un-inverting the mouse yolk sac suggests that the AX is equivalent to the region of yolk sac endoderm that later diverticulates to form the allantois (Fig. 12H). Intriguingly, tethering has been observed between the endodermal diverticulum of the allantois and the umbilical arteries in the human (Ingalls, 1920), suggesting that the yolk sac-derived allantoic diverticulum also undergoes an EMT event that was caught *in flagrante* prior to its resolution.

Finally, in light of Hedgehog's role in creating the placental vasculature, it is worth noting that some plant species consumed by humans contain compounds that behave like cyclopamine, which was discovered as a result of birth defects in sheep grazing on a certain type of lily (Heretsch et al., 2010), and which inhibit Hedgehog signaling. Resveratrol is a natural Hedgehog inhibitor of the epithelial-to-mesenchymal transition in cancer cells (Gao et al., 2015); it is found in peanuts, grapes and a variety of berries (Burns et al., 2002). Despite beneficial health effects for the mother (Baur and Sinclair, 2006), if received by the conceptus during early gestation, which relies upon hypoblast for early nutritional support (Freyer and Renfree, 2009), it is possible in light of results here that ingestion could lead to adverse effects in the development of the fetal-placental interface. Therefore, until studies are carried out to verify that this compound does not reach the human conceptus, it may be advisable to limit consumption of these products during the first few weeks of pregnancy to avoid possible insults on development of the umbilical and yolk sac vasculatures.

Acknowledgments

This study was made possible by pre-doctoral support from a General Medical Sciences grant under R25GM083252, T32 HD041921, and Advanced Opportunity grant (to A.M.R), and by grants from the March of Dimes (1-FY06-355, 1-FY09-511, and 6-FY12-271 to K.M.D), and the National Institutes of Child Health and Development (RO1 HD42706 and RO1 HD079481 to K.M.D). The authors are grateful to Dr. A.-K. Hadjantonakis for her generous contribution of the Transthyretin-CRE mouse line, to Kevin Eliceiri and Jayne Squirrell at LOCI (University of Wisconsin-Madison) for help with fluorescent optical imaging and use of the Spectral Lifetime Multiphoton Microscope; to Lauren Wierenga, Erin DeCloux, Jacob Daane, Ka Yi Ling, and Maria Mikedis for technical assistance; and to Peter Nichol and past members of the laboratory for helpful discussions during the preliminary stages of this study. The content of this manuscript is solely the responsibility of the authors and does not necessarily represent the official views of the National Institutes of Health.

References

Aumailley M, Timpl R. Attachment of cells to basement membrane collagen type IV. J Cell Biol. 1986; 103:1569–1575. [PubMed: 3771647]

Baur JA, Sinclair DA. Therapeutic potential of resveratrol: the in vivo evidence. Nat Rev Drug Discov. 2006; 5:493–506. [PubMed: 16732220]

Beddington RS. Toxigenics: strategic cell death in the embryo. Trends in Genetics. 1988; 4:1–2. [PubMed: 3238754]

Beddington RSP. An autoradiographic analysis of the potency of embryonic ectoderm in the 8th day postimplantation mouse embryo. J Embryol Exp Morph. 1981; 64:87–104. [PubMed: 7310311]

Beddington RSP. An autoradiographic analysis of tissue potency in different regions of the embryonic ectoderm during gastrulation in the mouse. J Embryol Exp Morph. 1982; 69:265–285. [PubMed: 7119671]

Beddington, RSP. Isolation, culture and manipulation of post-implantation mouse embryos. In: Monk, M., editor. Mammalian Development: A Practical Approach. IRL Press; Oxford: 1987. p. 43-70.

Beddington RSP. Induction of a second neural axis by the mouse node. Development. 1994; 120:613–620. [PubMed: 8162859]

Belaoussoff M, Farrington SM, Baron MH. Hematopoietic induction and respecification of A-P identity by visceral endoderm signaling in the mouse embryo. Development. 1998; 125:5009–5018. [PubMed: 9811585]

Bianchi DW, Wilkins-Haug LE, Enders AC, Hay ED. Origin of extraembryonic mesoderm in experimental animals: Relevance to chorionic mosaicism in humans. Am J Med Genet. 1993; 46:542–550. [PubMed: 8322818]

Bonnevie K. New facts on mesoderm formation and proamnion derivatives in the normal mouse embryo. J Morph. 1950; 86:495–546. [PubMed: 24537610]

Brewer S, Williams T. Finally, a sense of closure? Animal models of human ventral wall defects. Bioessays. 2004; 26:1307–1321. [PubMed: 15551266]

Burns J, Yokota T, Ashihara H, Lean ME, Crozier A. Plant foods and herbal sources of resveratrol. J Agric Food Chem. 2002; 50:3337–3340. [PubMed: 12010007]

Chen JK, Taipale J, Cooper MK, Beachy PA. Inhibition of Hedgehog signaling by direct binding of cyclopamine to Smoothened. Genes Dev. 2002; 16:2743–2748. [PubMed: 12414725]

Copp AJ, Roberts HM, Polani PE. Chimaerism of primordial germ cells in the early postimplanatation mouse embryo following microsurgical grafting of posterior primitive streak cells in vitro. J Embryol Exp Morph. 1986; 95:95–115. [PubMed: 3641878]

Corbel C, Salaun J, Belo-Diabangouaya P, Dieterlen-Lievre F. Hematopoietic potential of the pre-fusion allantois. Dev Biol. 2007; 301:478–488. [PubMed: 17010964]

Cordeiro MF, Guo L, Luong V, Harding G, Wang W, Jones HE, Moss SE, Sillito AM, Fitzke FW. Proc Natl Acad Sci. 2004; 101:13352–11356.

Cullen, TS. Embryology, Anatomy, and Diseases of the Umbilicus Together with Diseases of the Urachus. W B Saunders Company; Philadelphia: 1916.

Daane J, Enders AC, Downs KM. Mesothelium of the murine allantois exhibits distinct regional properties. J Morphology. 2011; 272:536–556.

Daane JM, Downs KM. Hedgehog signaling in the posterior region of the mouse gastrula suggests manifold roles in the fetal-umbilical connection and posterior morphogenesis. Dev Dyn. 2011; 240:2175–2193. [PubMed: 22016185]

Downs KM. Early placentation in the mouse. Placenta. 2002; 23:116–131. [PubMed: 11945078]

Downs, KM. Extraembryonic tissues. In: Stern, C., editor. Gastrulation. Cold Spring Harbor Press; Cold Spring Harbor: 2004. p. 449-459.

Downs KM. In vitro methods for studying vascularization of the murine allantois and allantoic union with the chorion. Methods Mol Med. 2006; 121:241–272. [PubMed: 16251748]

Downs KM. Systematic localization of Oct-3/4 to the gastrulating mouse conceptus suggests manifold roles in mammalian development. Dev Dyn. 2008; 237:464–475. [PubMed: 18213575]

Downs KM. Enigmatic primitive streak: prevailing notions and challenges concerning the body axis of mammals. Bioessays. 2009; 31:892–902. [PubMed: 19609969]

Downs KM, Bertler C. Growth in the pre-fusion murine allantois. Anat Embryol. 2000; 202:323–331. [PubMed: 11000283]

Downs KM, Davies T. Staging of gastrulation in mouse embryos by morphological landmarks in the dissection microscope. Development. 1993; 118:1255–1266. [PubMed: 8269852]

Downs KM, Gardner RL. An investigation into early placental ontogeny: allantoic attachment to the chorion is selective and developmentally regulated. Development. 1995; 121:407–416. [PubMed: 7768182]

Downs KM, Gifford S, Blahnik M, Gardner RL. Vascularization in the murine allantois occurs by vasculogenesis without accompanying erythropoiesis. Development. 1998; 125:4507–4520. [PubMed: 9778509]

Downs KM, Harmann C. Developmental potency of the murine allantois. Development. 1997; 124:2769–2780. [PubMed: 9226448]

Downs KM, Inman KE, Jin DX, Enders AC. The Allantoic Core Domain (ACD): New insights into development of the murine allantois and its relation to the primitive streak. Dev Dyn. 2009; 238:532–553. [PubMed: 19191225]

Dufort D, Schawartz L, Harpal K, Rossant J. The transcription factor HNF3ß is required in visceral endoderm for normal primitive streak morphogenesis. Development. 1998; 125:3015–3025. [PubMed: 9671576]

Dyer MA, Farrington SM, Mohn D, Munday JR, Baron MH. Indian hedgehog activates hematopoiesis and vasculogenesis and can respecify prospective neurectodermal cell fate in the mouse embryo. Development. 2001; 128:1717–1730. [PubMed: 11311154]

Eakin GS, Hadjantonakis AK, Papaioannou VE, Behringer RR. Developmental potential and behavior of tetraploid cells in the mouse embryo. Dev Biol. 2005; 288:150–159. [PubMed: 16246322]

Edwards GE, Miller RG, Phillips RA. Differentiation of rosette-forming cells from myeloid stem cells. J Immunol. 1970; 105:719–729. [PubMed: 4917253]

Elkabetz Y, Panagiotakos G, Al Shamy G, Socci ND, Tabar V, Studer L. Human ES cell-derived neural rosettes reveal a functionally distinct early neural stem cell stage. Genes and Development. 2008; 22:152–165. [PubMed: 18198334]

Enders AC, King BF. Formation and differentiation of extraembryonic mesoderm in the rhesus monkey. Am J Anat. 1988; 181:327–340. [PubMed: 3389303]

Eyal-Giladi H. Differentiation potencies of the young chick blastoderm as revealed by different manipulations. II. Localized damage and hypoblast removal experiments. J Embryol exp Morph. 1970; 23:739–749. [PubMed: 5528811]

Fernando P, Brunette S, Megeney LA. Neural stem cell differentiation is dependent upon endogenous caspase 3 activity. FASEB J. 2005; 19:1671–1673. [PubMed: 16103108]

Fernando P, Kelly JF, Balazsi K, Slack RS, Megeney LA. Caspase 3 activity is required for skeletal muscle differentiation. Proc Natl Acad Sci. 2002; 99:11025–11030. [PubMed: 12177420]

Freyer C, Renfree MB. The mammalian yolk sac placenta. J exp Zool. 2009; 312B:545–554.

Friedrich G, Soriano P. Promoter traps in embryonic stem cells: a genetic screen to identify and mutate developmental genes in mice. Genes Dev. 1991; 5:1513–1523. [PubMed: 1653172]

Gao Q, Yuan Y, Gan HZ, Peng Q. Resveratrol inhibits the hedgehog signaling pathway and epithelial-mesenchymal transition and suppresses gastric cancer invasion and metastasis. Oncology Letters. 2015; 9:2381–2387. [PubMed: 26137075]

Gardner RL. Investigation of cell lineage and differentiation in the extraembryonic endoderm of the mouse embryo. J Embryol exp Morph. 1982; 68:175–198. [PubMed: 7108421]

Gardner RL. Origin and differentiation of extraembryonic tissues in the mouse. Int Rev Exp Pathol. 1983; 24:63–143. [PubMed: 6302028]

Gardner RL, Rossant J. Investigation of the fate of 4.5 day post coitum mouse inner cell mass cells by blastocyst injection. J Embryol Exp Morph. 1979; 52:141–152. [PubMed: 521746]

Gekas C, Dieterlen-Lievre F, Orkin SH, Mikkola HKA. The placenta is a niche for hematopoietic stem cells. Dev Cell. 2005; 8:365–375. [PubMed: 15737932]

Gekas C, Rhodes KE, Van Handel B, Chhabra A, Ueno M, Mikkola HKA. Hematopoietic stem cell development in the placenta. Int J Dev Biol. 2010; 54:1089–1098. [PubMed: 20711986]

George WC. A presomite human embryo with chorda canal and prochordal plate. Carnegie Inst Contrib Embryol. 1942; 30:1–7.

Gerdes J, Schwab U, Lemke H, Stein H. Production of a mouse monoclonal antibody reactive with a human nuclear antigen associated with cell proliferation. Int J Cancer. 1983; 31:13–20. [PubMed: 6339421]

Gest TR, Carron MA. Embryonic origin of the caudal mesenteric artery in the mouse. Anat Rec. 2003; 271:192–201.

Gonzalez DM, Medici D. Signaling mechanisms of the epithelial-mesenchymal transition. Sci Signal. 2015; 7:re8.

Goodrich LV, Johnson RL, Milenkovic L, McMahon JA, Scott MP. Conservation of the hedgehog/patched signaling pathway from flies to mice: induction of a mouse patched gene by Hedgehog. Genes Dev. 1995; 10:301–312.

Grosse AS, Pressprich MF, Curley LB, Hamilton KL, Margolis B, Hildebrand JD, Gumucio DL. Cell dynamics in fetal intestinal epithelium: implications for intestinal growth and morphogenesis. Development. 2011; 138:4423–4432. [PubMed: 21880782]

Gudipaty SA, Lindblom J, Loftus PD, Redd MJ, Edes K, Davey CF, Krishnegowda V, Rosenblatt J. Mechanical stretch triggers rapid epithelial cell division through Piezo 1. Nature. 2017; 543:118–121. [PubMed: 28199303]

Hamilton DH, Litzinger MT, Fernando RI, Huang B, Palena C. Cancer vaccines targeting the epithelial-mesenchymal transition: tissue distribution of brachyury and other drivers of the mesenchymal-like phenotype of carcinomas. Semin Oncol. 2012; 39:358–366. [PubMed: 22595058]

Hatta K, Takagi S, Fujisawa M, Takeichi M. Spatial and temporal expression pattern of N-cadherin cell adhesion molecules correlated with morphogenetic processes of chicken embryos. Dev Biol. 1987; 120:215–227. [PubMed: 3817290]

Heretsch P, Tzagkaroulaki L, Giannis A. Cyclopamine and Hedgehog signaling: chemistry, biology, medical perspectives. Angew Chem Int Ed. 2010; 49:2–12. http://www.ics-mci.fr/mousecre/static_page/procedures.

Huh JR, Vernooy SY, Yu H, Yan N, Shi Y, Guo M, Hay BA. Multiple apoptotic caspase cascades are required in nonapoptotic roles for Drosophila spermatid individualization. PLoS Biology. 2004; 2:E15. [PubMed: 14737191]

Ingalls NW. A human embryo at the beginning of segmentation, with special reference to the vascular system. Contr Embryol Carnegie Inst No. 1920; 52:11.

Ingham PW, McMahon AP. Hedgehog signaling in animal development: paradigms and principles. Genes Dev. 2001; 15:3059–3087. [PubMed: 11731473]

Inman K, Downs KM. Localization of Brachyury (T) in embryonic and extraembryonic tissues during mouse gastrulation. Gene Exp Patterns. 2006a; 6:783–793.

Inman KE, Downs KM. Brachyury is required for elongation and vasculogenesis in the murine allantois. Development. 2006b; 133:2947–2959. [PubMed: 16835439]

Jurand A. Some aspects of the development of the notochord in mouse embryos. J Embryol Exp Morph. 1974; 32:1–33. [PubMed: 4141719]

Karhadkar SS, Bova GS, Abdallah N, Dhara S, Gardner DK, Maitra A, Isaacs JT, Berman DM, Beachy PA. Hegehog signallingin prostate regeneration, neoplasia and metastasis. Nature. 2004; 431:707–712. [PubMed: 15361885]

Kaufman, MH. The Atlas of Mouse Development. Academic Press; London: 1992.

Kinder SJ, Tsang TE, Quinlan GA, Hadjantonakis AK, Nagy A, Tam PPL. The orderly allocation of mesodermal cells to the extraembryonic structures and the anteroposterior axis during gastrulation of the mouse embryo. Development. 1999; 126:4691–4701. [PubMed: 10518487]

Köhler C, Orrenius S, Zhivotovsky B. Evaluation of caspase activity in apoptotic cells. J Immunol Methods. 2002; 265:97–110. [PubMed: 12072181]

Krishnamurthy K, Wang G, Rokhfeld D, Bieberich E. Deoxycholate promotes survival of breast cancer cells by reducing the level of pro-apoptotic ceramide. Breast Cancer Res. 2008; 10:R106. [PubMed: 19087284]

Kubo A, Shinozaki K, Shannon JM, Kouskoff V, Kennedy M, Woo S, Fehling JJ, Keller G. Development of definitive endoderm from embryonic stem cells in culture. Development. 2004; 131:1651–1662. [PubMed: 14998924]

Kunath T, Arnaud D, Uy GD, Okamoto I, Chureau C, Yamanaka Y, Heard E, Gardner RL, Avner P, Rossant J. Imprinted X-inactivation in extra-embryonic endoderm cell lines from mouse blastocysts. Development. 2005; 132:1649–1661. [PubMed: 15753215]

Kwon GS, Hadjantonakis AK. Transthyretin mouse transgenes direct RFP expression or Cre-mediated recombination throughout the visceral endoderm. Genesis. 2009; 47:447–455. [PubMed: 19415627]

Kwon GS, Viotti M, Hadjantonakis AK. The endoderm of the mouse embryo arises by dynamic widespread intercalation of embryonic and extraembryonic lineages. Dev Cell. 2008; 15:509–520. [PubMed: 18854136]

Lawson KA, Meneses J, Pedersen RA. Clonal analysis of epiblast fate during germ layer formation in the mouse embryo. Development. 1991; 113:891–911. [PubMed: 1821858]

Lee JD, Anderson KV. Morphogenesis of the node and notochord: the cellular basis for the establishment and maintenance of left-right asymmetry in the mouse. Dev Dyn. 2008; 237:3464–3476. [PubMed: 18629866]

Li F, He Z, Shen J, Huang Q, Li W, Liu X, He Y, Wolf F, Li CY. Apoptotic caspases regulate induction of iPSCs from human fibroblasts. Cell Stem Cell. 2010; 7:508–520. [PubMed: 20887956]

Li X, Deng W, Nail CD, Bailey SK, Kraus MH, Ruppert JM, Lobo-Ruppert SM. Snail induction is an early response to Gli1 that determines the efficiency of epithelial transformation. Oncogene. 2006

Maye P, Becker S, Kasameyer E, Byrd N, Grabel L. Hedgehog signaling in extraembryonic endoderm and ectoderm differentiation in ES embyroid bodies. Mech Dev. 2000; 94:117–132. [PubMed: 10842064]

McCann MR, Tamplin OJ, Rossant J, Séguin CA. Tracing notochord-derived cells using a Noto-cre mouse: implications for intervertebral disc movement. Disease Models Mech. 2012; 5:73–82.

Mesnard D, Guzman-Ayala M, Constam DB. Nodal specifies embryonic visceral endoderm and sustains pluripotent cells in the epiblast before overt axial patterning. Development. 2006; 133:2497–2505. [PubMed: 16728477]

Mikedis MM, Downs KM. Collagen type IV and perlecan exhibit concentrated and dynamic localization in the Allantoic Core Domain, a putative stem cell niche in the murine allantois. Dev Dyn. 2009; 238:3193–3204. [PubMed: 19924818]

Mikedis MM, Downs KM. STELLA-positive subregions of the primitive streak contribute to posterior tissues of the mouse gastrula. Dev Biol. 2012; 363:201–218. [PubMed: 22019303]

Mikedis MM, Downs KM. Widespread but tissue-specific patterns of interferon-induced transmembrane protein 3 (IFITM3, FRAGILIS, MIL-1) in the mouse gastrula. Gene Exp Patterns. 2013; 13:225–239.

Mikedis MM, Downs KM. Diverse roles for PRDM1/BLIMP1 in building the fetal-placental connection in the mouse gastrula. Dev Dyn. 2017; 246:50–71. [PubMed: 27696611]

Miura M. Apoptotic and nonapoptotic caspase functions in animal development. Cold Spring Harbor Persp Biol. 2012; 4:a008664.

Mossman HW. Comparative morphogenesis of the fetal membranes and accessory uterine structures. Contr Embryol. 1937; 26:133–247.

Nagy A, Gocza E, Diaz EM, Prideaux VR, Ivanyi E, Markkula M, Rossant J. Embryonic stem cells alone are able to support fetal development in the mouse. Development. 1990; 110:815–821. [PubMed: 2088722]

Naiche LA, Arora R, Kania A, Lewandoski M, Papaioannou VE. Identity and fate of Tbx4-expressing cells reveal develomental cell fate decisions in the allantois, limb, and external genitalia. Dev Dyn. 2011 in press.

Naiche LA, Papaioannou VE. Loss of *Tbx4* blocks hindlimb development and affects vascularization and fusion of the allantois. Development. 2003; 130:2681–2693. [PubMed: 12736212]

Naiche LA, Papaioannou VE. Cre activity causes widespread apoptosis and lethal anemia during embryonic development. Genesis. 2007; 45:768–775. [PubMed: 18064676]

North TE, deBruijn MF, Stacy T, Talebian L, Lind E, Robin C, Binder M, Dzierzak E, Speck NA. Runx1 expression marks long-term repopulating hematopoietic stem cells in the midgestation mouse embryo. Immunity. 2002; 16:661–672. [PubMed: 12049718]

North TE, Gu TL, Stacy T, Wang Q, Howard L, Binder M, Marin-Padilla M, Speck NA. Cbfa2 is required for the formation of intra-aortic hematopoietic clusters. Development. 1999; 126:2563–2575. [PubMed: 10226014]

O'Rahilly, R. Developmental stages in human embryos Part A: Embryos of the first three weeks (Stages 1-9). Vol. 631. Carnegie Institution; Washington DC: 1973. p. 1-167.

Odent S, Atti-Bitach T, Blayau M, Mathieu M, Aug J, De Delezo AL, Gall JY, Le Marec B, Munnich A, David V, Vekemans M. Expression of the Sonic hedgehog (SHH) gene during early human development and phenotypic expression of new mutations causing holoprosenchephaly. Hum Mol Genet. 1999; 8:1683–1689. [PubMed: 10441331]

Otterbach K, Dzierzak E. The murine placenta contains hematopoietic stem cells within the vascular labyrinth region. Dev Cell. 2005; 8:377–387. [PubMed: 15737933]

Palis J. Yolk-sac hematopoiesis: the first blood cells of mouse and man. Exp Hematol. 2001; 29:927–936. [PubMed: 11495698]

Park Y, Rangel C, Reynolds MM, Caldwell MC, Johns M, Nayak M, Welsh CJ, McDermott S, Datta S. Drosophila perlecan modulates FGF and hedgehog signals to activate neural stem cell division. Dev Biol. 2003; 253:247–257. [PubMed: 12645928]

Perez-Garijo A, Martín FA, Morata G. Caspase inhibition during apoptosis causes abnormal signalling and developmental aberrations in Drosophila. Development. 2004; 131:5591–5598. [PubMed: 15496444]

Perron M, Boy S, Amato MA, Viszian A, Koebernick K, Pieler T, Harris WA. A novel function for Hedgehog signaling in retinal pigment epithelium differentiation. Development. 2003; 130:1565–1577. [PubMed: 12620982]

Pokutta S, Weis WI. Structure and mechanism of cadherins and catenins in cell-cell contacts. Annu Rev Cell Dev Biol. 2007; 23:237–261. [PubMed: 17539752]

Rodriguez AM, Jin DX, Wolfe AD, Mikedis MM, Wierenga L, Hashmi M, Viebahn C, Downs KM. Brachyury drives formation of a distinct vascular branchpoint critical for fetal-placental arterial union in the mouse gastrula. Dev Biol. 2017 in press.

Selleck MA, Stern CD. Fate mapping and cell lineage analysis of Hensen's node in the chick embryo. Development. 1991; 112:615–626. [PubMed: 1794328]

Shook D, Keller R. Mechanisms, mechanics and function of epithelial-mesenchymal transitions in early development. Mech Dev. 2003; 120:1351–1383. [PubMed: 14623443]

Singleton CD, Casagrande VA. A reliable and sensitive method for fluorescent photoconversion. J Neurosci Methods. 1996; 64:47–54. [PubMed: 8869483]

Snell, GB., Stevens, LC. Early embryology. In: Green, EL., editor. Biology of the Laboratory Mouse. McGraw Hill; New York: 1966. p. 205-245.

Snow MHL. Gastrulation in th emouse: growth and regionalisation of the epiblast. J Embryol Exp Morph. 1977; 42:293–303.

Stern CD, Downs KM. The hypoblast (visceral endoderm): an evo-devo perspective. Development. 2012; 139:1059–1069. [PubMed: 22354839]

Stevenson BR, Siliciano JD, Mooseker MS, Goodenough DA. Identification of ZO-1: a high molecular weight polypeptide associated with the tight junction (zonula occludens) in a variety of epithelia. J Cell Biol. 1986; 103:755–766. [PubMed: 3528172]

Stevenson, RE., Hall, JG. Human malformations and related anomalies. Oxford University Press; Oxford: 2006.

Stower MJ, Srinivas S. Heading forwards: anterior visceral endoderm migration in patterning the mouse embryo. Phil Trans R Soc Lond B Biol Sci. 2014; 369

Sulik K, Dehart DB, Inagaki JL, Vrablic CT, Gesteland K, Schoenwolf GC. Morphogenesis of the murine node and notochordal plate. Dev Dyn. 1994; 201:260–278. [PubMed: 7881129]

Tam PPL, Beddington RSP. The formation of mesodermal tissues in the mouse embryo during gastrulation and early organogenesis. Development. 1987; 99:109–126. [PubMed: 3652985]

Tarkowski AK, Witkowska A, Opas J. Development of cytochalasin B-induced tetraploid and diploid/tetraploid mosaic mouse embryos. J Embryol exp Morph. 1977; 41:47–64. [PubMed: 591878]

Thomas PQ, Beddington R. Anterior primitive endoderm may be responsible for patterning the anterior neural plate in the mouse embryo. Curr Biol. 1996; 6:1487–1496. [PubMed: 8939602]

Thomas PQ, Brown A, Beddington RS. Hex: a homeobox gene revealing peri-implantation asymmetry in the mouse embryo and an early transient marker of endothelial cell precursors. Development. 1998; 125:85–94. [PubMed: 9389666]

Tiapale J, Chen JK, Cooper MK, Wang B, Mann RK, Milenkovic L, Scott MP, Beachy PA. Effects of oncogenic mutations in Smoothened and Patched can be reversed by cyclopamine. Nature. 2000; 406:1005–1009. [PubMed: 10984056]

Wilkinson DG, Bhatt S, Herrmann BG. Expression pattern of the mouse T gene and its role in mesoderm formation. Nature. 1990; 343:657–659. [PubMed: 1689462]

Wolfe AD, Downs KM. Mixl1 localizes to putative axial stem cell reservoirs and their posterior descendants in the mouse. Gene Exp Patterns. 2014; 15:8–20.

Wolfe AD, Rodriguez AM, Downs KM. STELLA collaborates in distinct mesendodermal cell subpopulations at the fetal-placental interface in the mouse gastrula. Dev Biol. 2017; 425:208–222. [PubMed: 28389228]

Xu Y, Xiao R, Li Y. Effect of ethanol on the development of visceral yolk sac. Hum Reprod. 2005; 20:2509–2516. [PubMed: 15905295]

Zeigler BM, Sugiyama D, Chen M, Guo Y, Downs KM, Speck NA. The allantois and chorion, which are isolated before circulation or chorio-allantoic fusion have hematopoietic potential. Development. 2006; 133:4183–4192. [PubMed: 17038514]

Zhang SC. Neural subtype specification from embryonic stem cells. Brain Pathology. 2006; 16:132–142. [PubMed: 16768754]

Zhu J, Kwan KM, Mackem S. Putative oncogene Brachyury (T) is essential to specify cell fate but dispensable for notochord progenitor proliferation and EMT. Proc Natl Acad Sci. 2016; 113:3820–3825. [PubMed: 27006501]

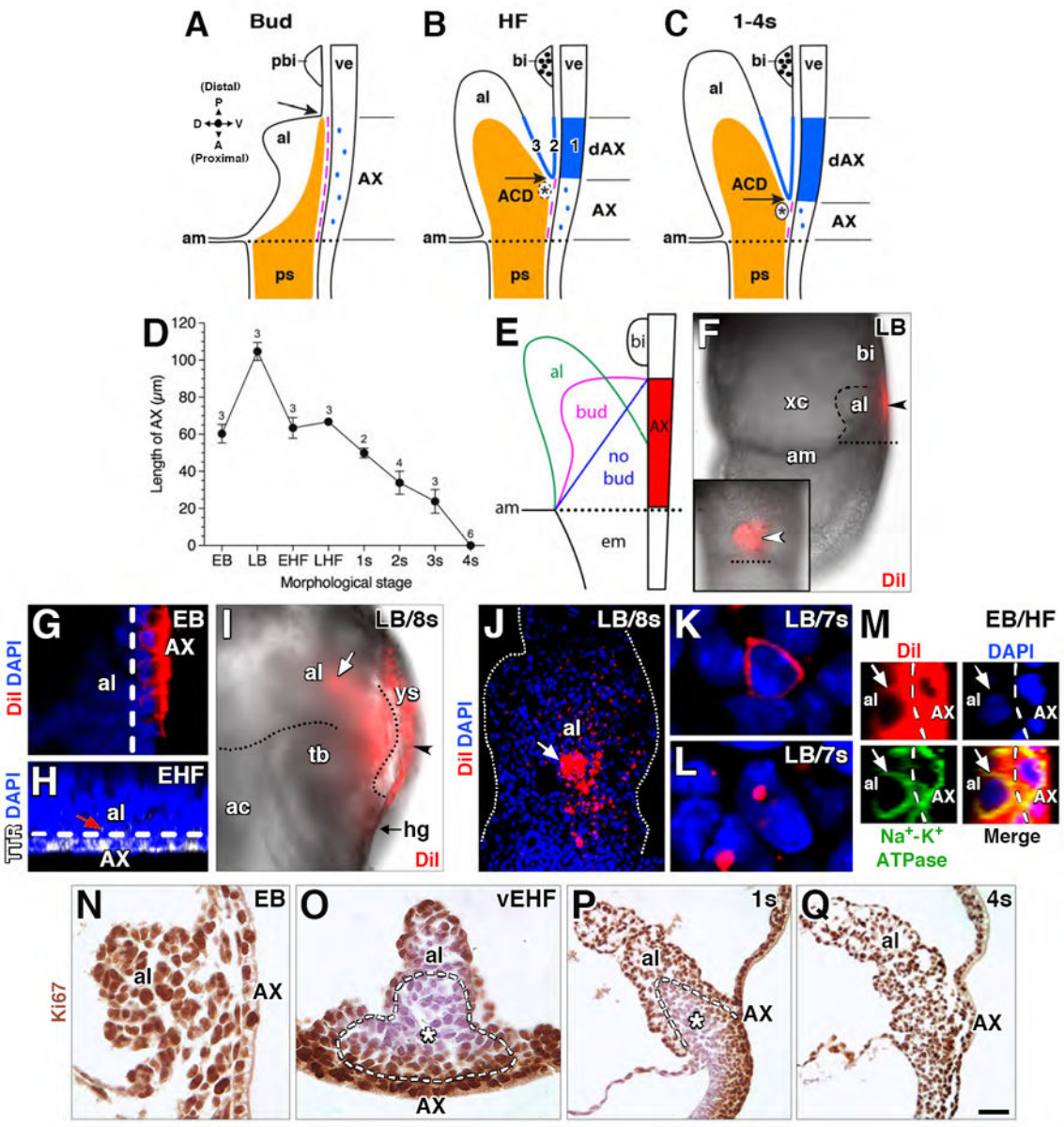

Figure 1. Working model and DiI-fate mapping the AX *in situ*

(**A-C**) Schematic diagram, mid-sagittal plane of the posterior embryonic-extraembryonic interface over time. Compass: posterior/distal (P), anterior/proximal (A), dorsal (D) and ventral (V). Modified, with permission from (Rodriguez et al., 2017). Spatiotemporal *Ptch1* expression in this region was previously described (Daane and Downs, 2011), particularly the *Ptch1*-negative AX domain (Figs 1L, 2G of that study). (**A**) The primitive streak (ps; orange) reaches beyond the embryonic-extraembryonic boundary (dotted line) stopping short of the prospective blood islands (pbi), and defining the allantoic-yolk sac junction (black arrow). AX, separated from the streak by a continuous basement membrane (magenta), exhibits low *Ptch1* (blue dots). (**B**) The ps expands into the allantoic core domain (ACD; orange); the nascent vessel of confluence (discontinuous black oval, asterisk) forms at the allantoic-yolk sac junction (black arrow), which has shifted anteriorly. High *Ptch1*

(solid blue) is now evident in distal AX (dAX; 1); yolk sac mesothelium (2); and ventral allantoic wall (3). Blood islands (bi) are present. Basement membrane (magenta line) between the streak and AX is discontinuous. (**C**) Mature vessel of confluence and further anterior progression of the allantoic-yolk sac junction. (**D**) Decreasing AX length with increasing morphological stage. Mean ± SEM with sample sizes. (**E**) Schematic diagram, contact between AX and allantois changes over time. Dotted line, embryonic-extraembryonic boundary. (**F**) Left side view (main panel) and frontal (ventral) view (inset), whole mount specimen (LB stage), restriction of initial DiI label (arrowheads) to the extraembryonic region (dotted line, embryonic-extraembryonic boundary). Dashed line delineates allantoic bud. (**G**) Sagittal optical section, specificity of initial DiI label to AX. Dashed line delineates AX. (**H**) Transverse slice through reconstructed z-stack; transthyretin (TTR) throughout AX with occasional punctate spots in allantois (red arrow), to where it was likely secreted. Dashed line delineates AX. (**I**) Left side view, whole mount specimen, fetal-placental interface, Di-labeled post-culture conceptus; fluorescent DiI visible on visceral yolk sac (arrowhead) and spreading into allantois (white arrow). Dotted lines delineate ventral and dorsal surface of allantois. (**J**) Frontal optical section of specimen in **I**, after removal of the visceral yolk sac, DiI label (white arrow, red color) in the allantois (white dots outline allantois). (**K, L**) Enlarged examples of DiI label in AX-derived mesodermal cells: fully covered (**K**), dotted (**L**). (**M**) Sagittal slice, reconstructed z-stack, displaying co-localization of DiI with the plasma membrane protein, Na^+-K^+ ATPase, in both the AX and its mesodermal derivatives within the allantois. (**N-Q**) Histological sections, Ki67-immunostained allantois (mid-sagittal, **N, P, Q**; transverse, **O**); with the exception of the headfold (**O**) and early somite stages (**P**), where cells within allantoic core are largely quiescent, allantoic cells in contact with the AX and the AX itself are proliferative. ACD, white asterisk and outlined by white dashed lines (**O, P**). Scale bar (**Q**): 3 μm (**K, L**); 7μm (**M**); 10 μm (**G, H, N**); 20 μm (**O**); 30 μm (**J**); 50 μm (**P, Q**); 100 μm (**F, I**); 150 μm (**F** inset). ac, amniotic cavity; al, allantois; am, amnion; bi, blood island; em, embryo; hg, hindgut; tb, tailbud; ve, visceral endoderm; xc, exocoelomic cavity; ys, yolk sac.

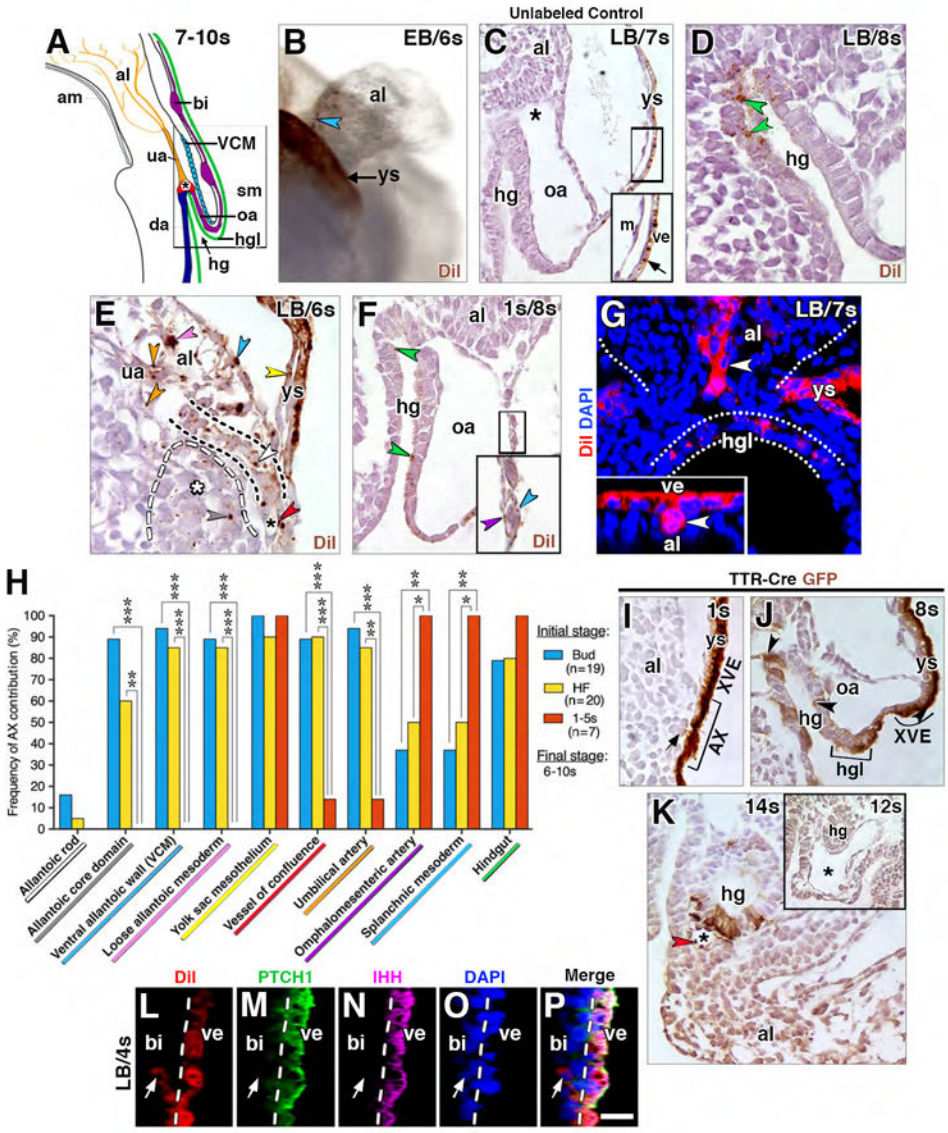

Figure 2. Contribution of AX to the fetal-placental interface

(**A**) Structures encompassed within the fetal-placental interface, color coded to match results of fate mapping in panel **H**. Boxed region, structures that form a developmental continuum of those related to the nascent allantoic-yolk sac junction (see text). (**B**) Oblique ventral/side view, DiI-labeled whole mount specimen after culture and photobleaching shows contribution to the allantoic ventral wall (brown, blue arrowhead), visible after reflexion of overlying yolk sac (brown, background staining). (**C-F**) Sagittal histological sections through allantoic-yolk sac junction (**E**) and fetal-placental interface (**C, D, F**) showing a photobleached unlabeled cultured control (**C**) and cultured DiI-labeled specimens (**D-F**). Unlabeled photobleached control exhibits background staining limited to visceral endoderm (arrow in **C** inset, which is enlargement of main panel's boxed region). Positive labeling (color-coded arrowheads): hindgut (**D**, **F**, green), umbilical artery (**E**, orange), loose allantoic mesoderm (**E**, pink), ventral allantoic wall (**E**, blue), yolk sac mesoderm (**E**,

yellow), allantoic rod (**E**, white; outlined by black dashed line), allantoic core domain (**E**, grey, the region of which is indicated by white asterisk and outlined by white dashed line); vessel of confluence (**E**, red; black asterisk); splanchnic mesoderm (**F**, blue, inset of boxed region in larger panel); and omphalomesenteric artery (**F**, inset, purple). (**G**) Frontal optical section of the proximal-most region of the allantois of a DiI labeled specimen after culture with AX contribution to the allantoic rod-like structure (white arrowhead). The distal region, not shown, resembles the profile shown in panel E. Inset, rod-like structure (whitle arrowhead) in a transvers slice through reconstructed z-stack, at the level of white arrowhead in main panel. White dots outline allantois and hindgut lip. (**H**) Frequency of AX contribution to structures within the allantoic-yolk sac junction and fetal-placental interface; significance: Fisher's exact test: *, $P < 0.05$; **, $P < 0.01$; ***, $P < 0.001$; the key along the X-axis is color-coded to match the color-coded arrowheads in panels **C-G**. (**I-J**) Sagittal (**I, J**) and transverse (**K**, and inset) histological sections through the fetal-placental interface of TTR-Cre-positive specimens (**I-K**) and a TTR-CRE-negative control specimen (inset, **K**) immunostained with anti-GFP. Brown staining is limited to Cre-positive specimens (**I-J**). Staining is continuous throughout extraembryonic visceral endoderm (XVE, **I, J**), including the AX (**I**), but it is mosaic in the hg (**J**, arrowheads; **K**) as well as in the hindgut lip (**J**, bracketed region). Arrow (**I**) indicates a mesodermal cell underlying the AX with slight brown staining. Brown staining is present in extraembryonic mesodermal tissues at 11-14s, including the VOC (asterisk, **K**; red arrowhead) and allantois (**K**). (**L-P**) Sagittal slice through reconstructed z-stack, DiI-labeled blood island-associated visceral endoderm co-localizes PTCH1 and IHH and makes negligible contributions to the mesoderm. Dashed line delineates yolk sac visceral endoderm. Scale bar (**O**): 10 μm (**D, L-P**); 15 μm (**B, E, G**); 20 μm (**F, J**); 35 μm (**C**); 43 μm (**K, K** inset). al, allantois; am, amnion; bi, blood island; da, dorsal aortae; hg, hindgut; hgl, hindgut lip; m, mesothelium; oa, omphalomesenteric artery; sm, splanchnic mesoderm; ua, umbilical artery; VCM, ventral cuboidal mesothelium; ve, visceral endoderm; ys, yolk sac.

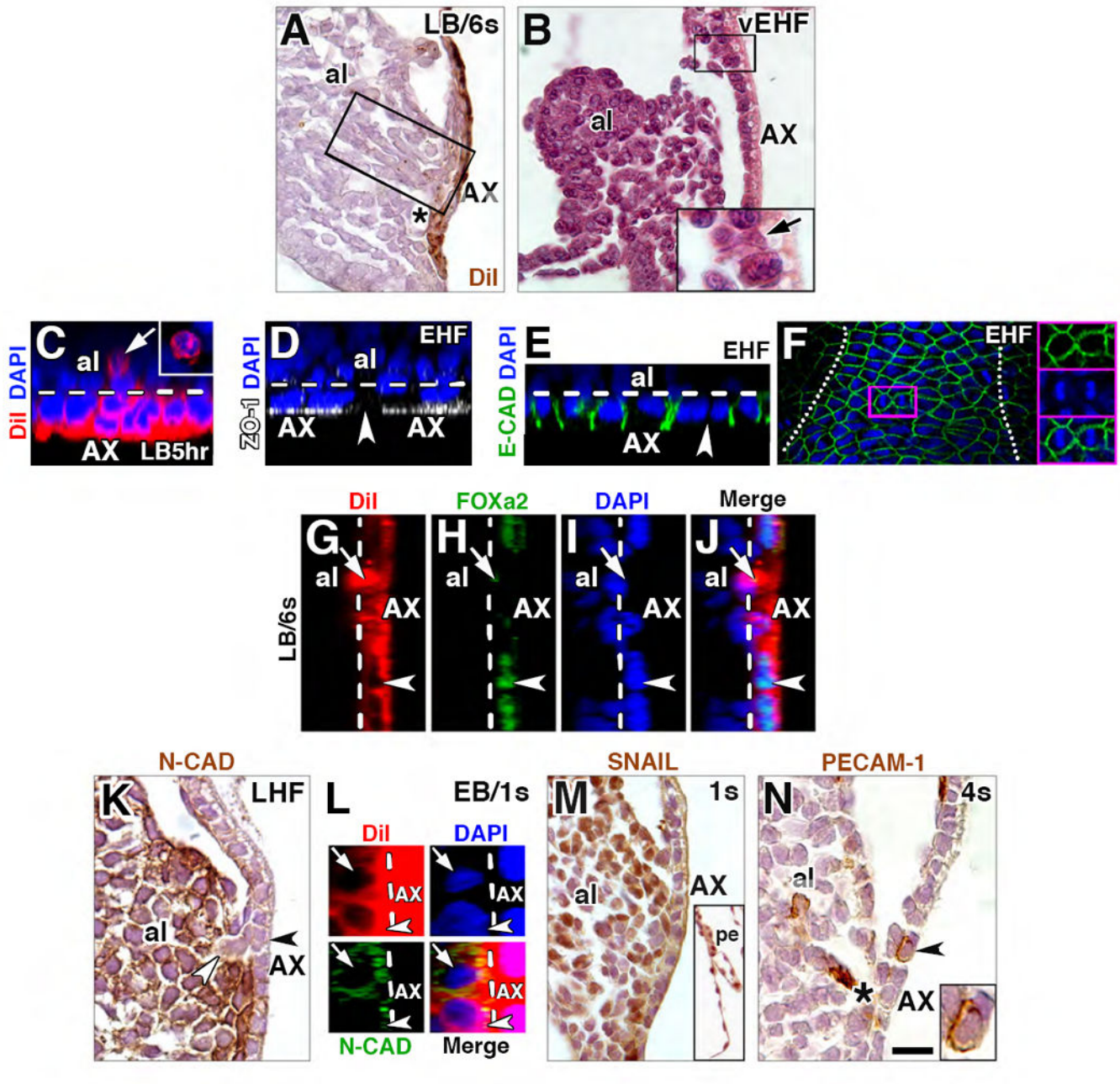

Figure 3. AX contributes to mesoderm via an epithelial-to-mesenchymal transition (EMT)

(**A**) Sagittal histological section, DiI-labeled cells streaming from the AX (boxed region) following culture and photobleaching. Black asterisk, vessel of confluence. (**B**) Sagittal histological section, allantoic bud, AX cell (arrow) extending basally into the allantois at the allantoic-yolk sac junction (enlarged in inset). The virtual space between allantoic bud and AX is a fixation and histological processing artifact. (**C**) Transverse slice, reconstructed z-stack of the AX, round DiI-covered/AX-derived cell (arrow, enlarged in inset from frontal optical section) that has been liberated from AX (delineated by the white dashed line) after 5 hours of culture. (**D**) Transverse slice, reconstructed z-stack, gap in axial continuity of ZO-1

(arrowhead) within AX (white dashed line). (**E**) Transverse slice, reconstructed z-stack, loss of junctional E-CADHERIN (arrowhead) between AX cells; white dashed line delineates the AX's epithelium. (**F**) Frontal optical section, AX, E-CADHERIN-immunostained AX overlying the allantois (the extent of which is indicated by the white dots), highlighting mitotic profile in axial midline (magenta-outlined box), enlarged in insets on the right, showing individual channels (top, middle boxes) as well as merged image (bottom box). (**G-J**) Sagittal slice, reconstructed z-stack, of an exiting DiI-labeled AX-derived cell (arrow) which exhibits spotty FOXa2 staining; nuclei of remaining AX cells are robustly FOXa2-positive (arrowhead; AX, white dashed line). (**K**) Sagittal histological section, continuity between two N-CAD-negative cells, one of which remains within AX (black arrowhead) and the other has just departed (white arrowhead), entering the generally N-CAD-positive allantois. (**L**) Sagittal slice, reconstructed z-stack, exhibiting relatively little (bottom cell, arrowhead) or robust (top cell, arrow) N-CAD, while AX (dashed white line), is N-CAD-negative. (**M**) Sagittal histological section, SNAIL in allantois and parietal endoderm (inset), but not in AX or other visceral endoderm. (**N**) Sagittal histological section, rounded PECAM-1-positive AX cell (arrowhead, enlarged in inset). Black asterisk, VOC. Scale bar (**N**): 7 μm (**C**-E, **G-J, L**); 13 μm (**K**); 20 μm (**B, N**); 30 μm (**F**); 40 μm (**A, M, M** inset). al, allantois; pe, parietal endoderm.

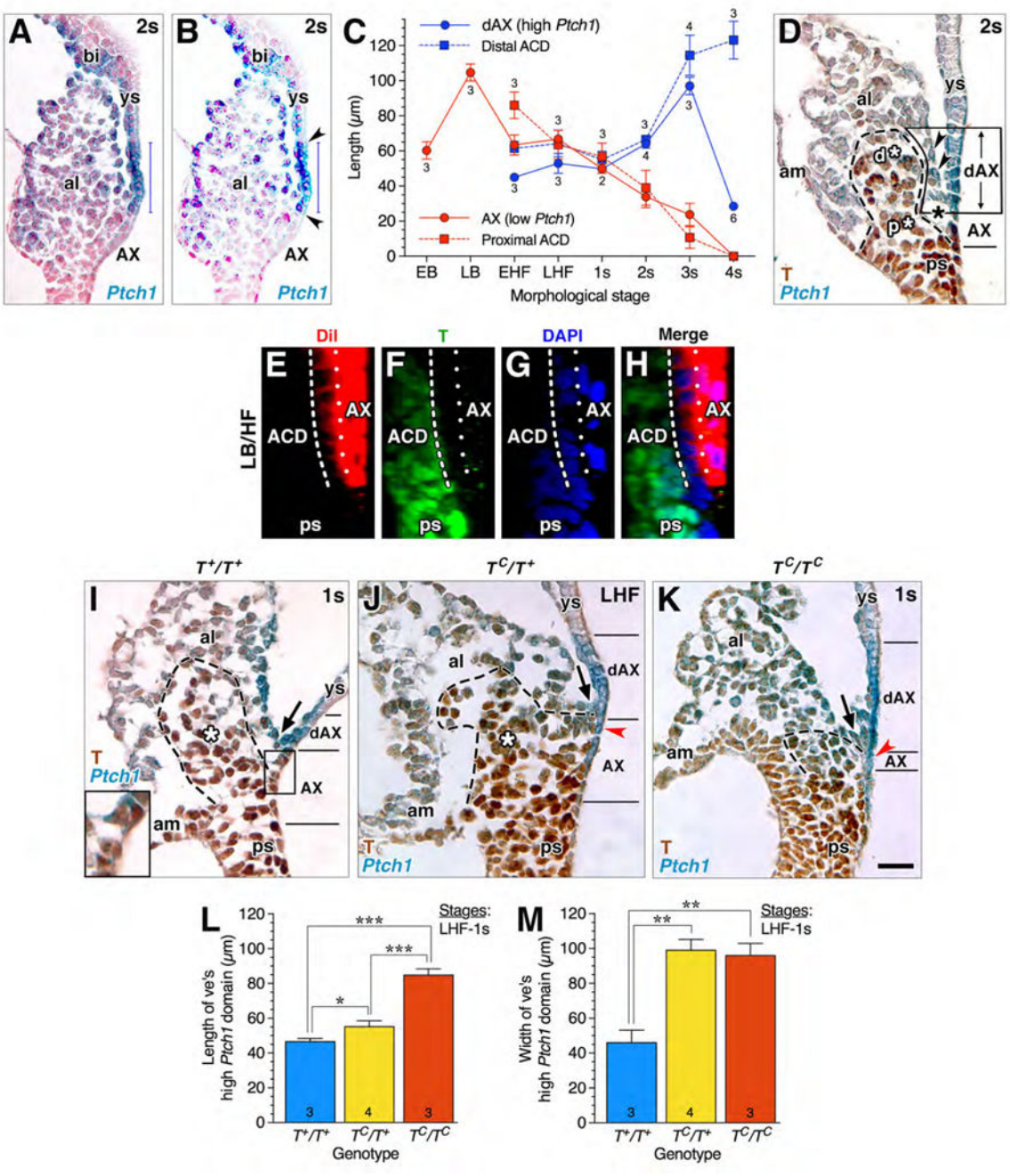

Figure 4. High *Ptch1* in visceral endoderm following loss of contact with the primitive streak

(**A, B**) Thresholding determined the length of high *Ptch1* domain. Vertical blue lines in each panel are the ruler provided by NIS Elements. Sagittally-oriented histological section through *Ptch1*$^{+/-}$ reporter (2s stage, ~E8.25) (**A**). The same specimen (**B**) with "thresholding" to enhance the high Ptch1 domain in the dAX and confirm its borders (arrowheads). (**C**) Inverse relationship between AX (low *Ptch1*)/proximal ACD; red), and dAX (high *Ptch1*)/distal ACD; blue) at increasing morphological stages. Mean ± SEM, sample sizes above data points for T-stained material used to measure ACD length, and below for *Ptch1:lacZ* X-gal stained material used to measure AX and dAX length. (**D**)

Sagittal histological section, allantois, showing a wedge of mesoderm within allantoic ventral wall (arrowheads) that now separates high *Ptch1* dAX (formerly the low *Ptch1* AX) from the largely T-positive ACD. The dAX is associated with the distal ACD (d*) and the AX is associated with the proximal ACD (p*). (**E-H**) Sagittal slice, reconstructed z-stack, AX-derived mesodermal cells have intervened between the AX and T-defined ACD, indicated by white dotted and dashed lines, respectively. (**I-K**) Sagittal histological sections of T-immunostained $T^{C}/_{Ptch1}$ littermates showing limits of high and low *Ptch1* domains in each genotype; the arrow in all three panels indicates the allantoic-yolk sac junction, which separates the dAX from the AX. (**I**) wildtype specimen sagittally oblique; low *Ptch1* in AX (boxed) is enlarged in inset. (**J, K**) Primitive streak is breaking down in the heterozygotes (**J**) and homozygotes (**K**), as indicating by decreasing levels of T, with overlying *Ptch1* as high as in the dAX (red arrowheads). (**L**) Mean length ± SEM of high *Ptch1* domain; sample sizes indicated. Significance: Student t-Test: *, $P < 0.05$; ***, $P < 0.001$. (**M**) Mean width ± SEM of high *Ptch1* domain; sample sizes indicated. Significance: Student t-Test: **, $P < 0.01$. Scale bar (**K**): 16 μm (**E-H**); 25 μm (**D, I-K**). al, allantois; am, amnion; ps, primitive streak; ve, visceral endoderm; ys, yolk sac.

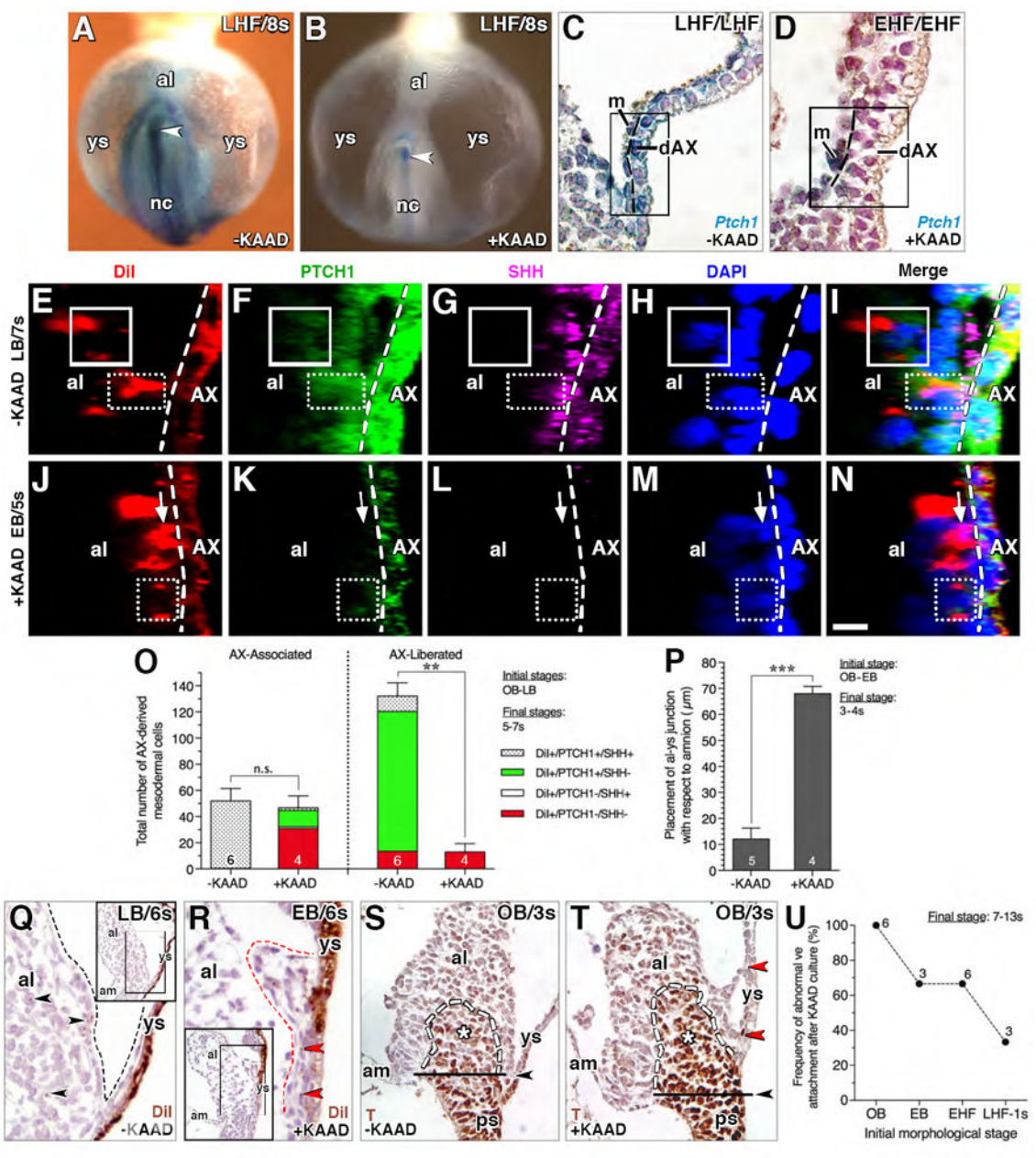

Figure 5. Loss of *Ptch1* reduces mesodermal allocation by preventing resolution of the EMT in the AX

(**A, B**) Frontal (ventral) views, X-gal-stained whole mount *Ptch1:lacZ* reporter conceptuses after culture: **A**, untreated control (-KAAD), **B**, KAAD-cyclopamine-treated (+KAAD). Arrowhead, *Ptch1* in posterior notochord. (**C, D**) Sagittal histological section, dAX, *Ptch1:lacZ* reporter conceptuses showing high *Ptch1* in the untreated control (**C**), and loss of *Ptch1* in dAX (**D**) after 4 hours of KAAD treatment. Boxed region, yolk sac mesothelium with residual *Ptch1*, and multilayering of the dAX, delineated by dashed line. (**E-N**) Sagittal slice, reconstructed z-stack, DiI labeled/AX-derived mesodermal cells (left of white dashed line, AX boundary) normally exhibit both SHH and PTCH1 when associated with AX (solid

box, **E-I**) and only PTCH1 (dotted box, **E-I**) once liberated from AX; upon KAAD-treatment, AX-derived cells remain largely associated with AX, exhibiting only PTCH1 (dotted box, **J-N**) or neither PTCH1 or SHH (arrow). (**O**) Number of DiI-labeled AX-derived mesodermal cells in untreated and KAAD-treated specimens, categorized as AX-associated, i.e., in contact with the AX, and AX-liberated, i.e., fully disengaged from the AX. Mean ± SEM and sample sizes. Significance: Student t-Tests;: n.s., not significant with $P = 0.623$; **, $P < 0.01$. (**P**) Placement of allantoic-yolk sac junction with respect to amnion in -KAAD and +KAAD specimens; mean ± SEM and sample sizes. Significance: Student t-Tests; ***, $P < 0.001$. (**Q, R**) Sagittal histological sections, DiI-photobleached allantois KAAD-treated initially at bud stages and cultured through 6s. These compare normal tissue separation at the allantoic-yolk sac junction (black dashed line, **Q**) of untreated controls with the abnormal clumping between the allantois and yolk sac (red dashed line, **R**) after KAAD-treatment. Black arrowheads (**Q**), AX-derived cells fully liberated from the AX in the untreated specimens; red arrowhead (**R**), immobilized AX-derived cells that have not been liberated from the AX in the absence of Hedgehog. Main panels are enlargements of boxed region in insets. (**S, T**) Sagittal histological sections comparing untreated (**S**) and KAAD-treated (**T**) pre-bud (no allantoic bud, OB) conceptuses, both of which exhibit normal localization of T. Black arrowheads (**S, T**), correct placement of allantoic-yolk sac junction (**S**) and where it should have been in the KAAD-treated specimens (**T**). Red arrowheads (**T**), abnormal connections between the dAX and allantois. (**U**) Frequency of abnormal visceral endoderm (ve) attachments after KAAD culture at increasing initial morphological stages, with sample sizes. Scale bar (**N**): 10 μm (**E-N**); 18 μm (**C, D**); 35 μm (**Q, R**); 40 μm (**S, T**); 100 μm (**A, B**). al, allantois; am, amnion; m, mesothelium; nc, notochord; ps, primitive streak; ys, yolk sac.

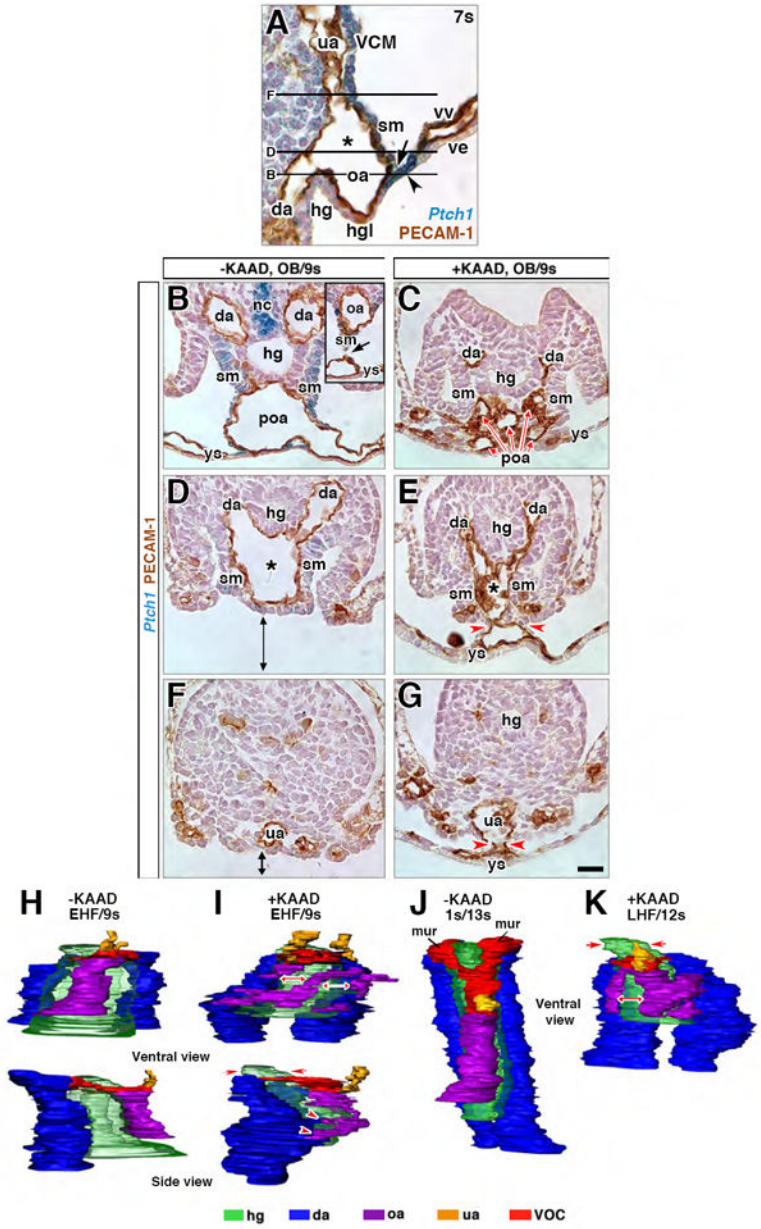

Figure 6. Abnormal structural organization of the fetal-placental interface in the absence of Hedgehog

(**A**) Sagittal PECAM-1-immunostained histological section, fetal-placental interface, 7s-stage *Ptch1:lacZ* reporter conceptus. The allantoic-yolk sac junction is defined by the dAX (black arrowhead) and splanchnic mesoderm (sm; black arrow) continuous with the ventral allantoic wall (VCM). High *Ptch1* localizes to VCM, sm, and dAX. The umbilical artery (ua), omphalomesenteric artery (oa), and dorsal aortae (da) have united at the vessel of confluence (asterisk). The hindgut lip (hgl) expresses relatively low *Ptch1*. Horizontal lines indicate the planes of section illustrated in **B-G**. (**B-G**) Transverse PECAM-1-immunostained histological sections of untreated (-KAAD; **B, D, F**) and KAAD-treated (+KAAD; **C, E, G**) specimens, taken at the level equivalent to the lines indicated in A.

Black arrow (**B** inset), site where omphalomesenteric artery is released from the vitelline vasculature. Red arrows (**C**), prospective omphalomesenteric artery (poa) presented as multiple vessels. Double arrows (**D, F**) indicate that vessel of confluence (**D**, black asterisk) and umbilical artery (ua, **F**) are separated from the vitelline vasculature in the untreated specimens. Red arrowheads (**E, G**) indicate that the vessel of confluence (asterisk, **E**) and ua (**G**) remain tethered to the vitelline vasculature in KAAD-treated specimens. (**H-K**) 3D models reconstructed from PECAM-1-immunostained arterial vessels and associated hindgut at the posterior embryonic-extraembryonic interface prior to (**H-I**) or during (**J-K**) early remodeling of the vessel of confluence. Color key indicated below panels. Red double arrows (**I, K**) indicate abnormal gaps between the multiple vessels that appear to comprise the “oa”; red arrowheads (**I**) are aberrant connections between the oa and dorsal aortae (da); red arrows (**I, K**) indicate abnormal positioning of the hindgut (hg) distal to the vessel of confluence. Scale bar (**G**): 18 μm (**A**); 25 μm (**D-G**); 30 μm (**B**, **C**). al, allantois; mur, medial umbilical roots; nc, notochord; vv, vitelline blood vessels; ys, yolk sac.

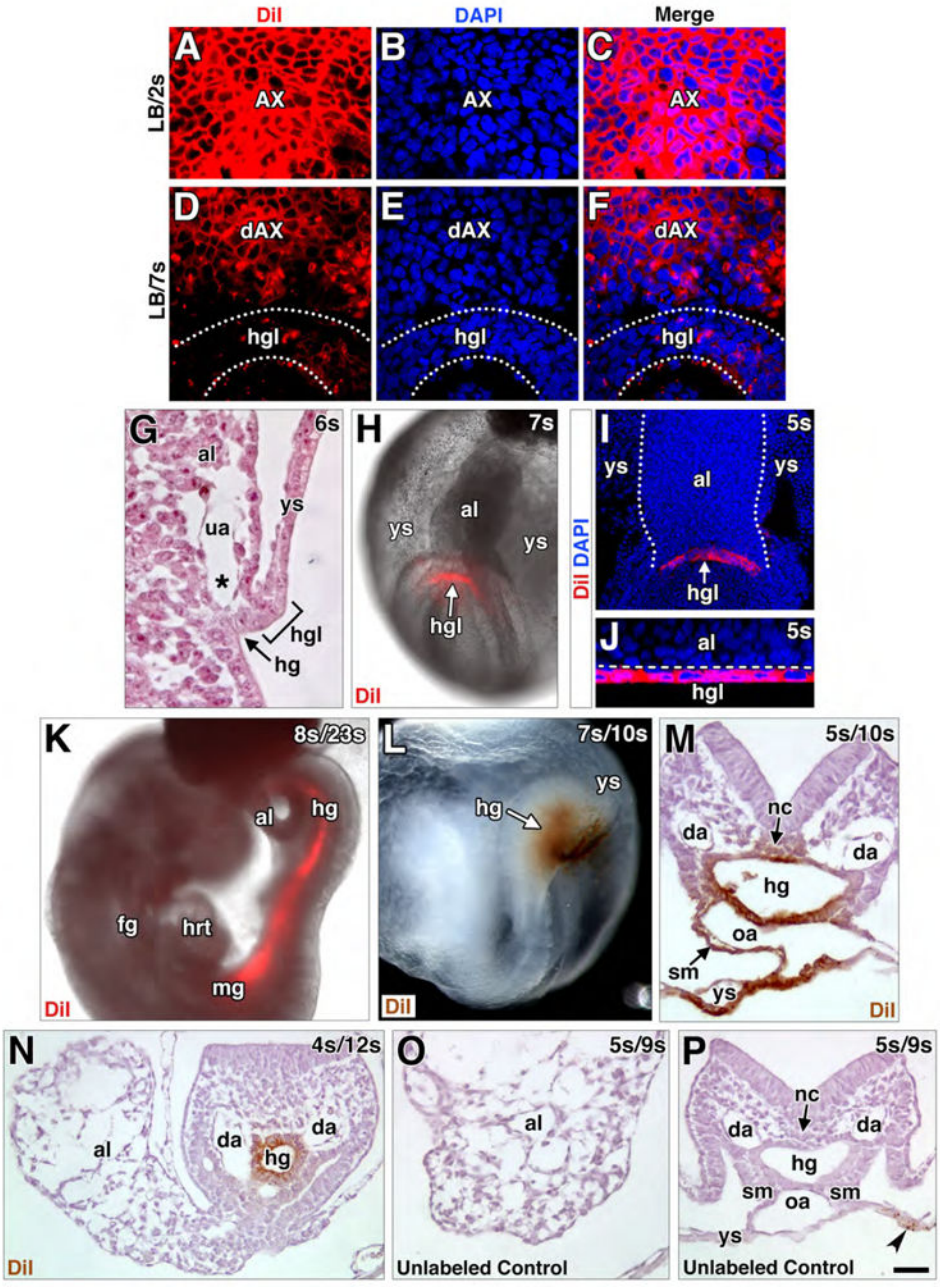

Figure 7. The hindgut lip, formed by the AX, is a mesendodermal tissue

(**A-F**) Frontal (ventral) optical sections through AX (**A-C**) or dAX and hindgut lip (**D-F**). After short culture, DiI is undiluted in AX (**A-C**). After culture to later stages (**D-F**), dAX is largely uniformly labeled due to attenuation of its EMT, while the hindgut lip (hgl; outlined by dotted white lines), contiguous with the dAX, exhibits salt-and-pepper-like DiI, in accord with previous EMT activity and exhaustion of the label. (**G**) Sagittal histological section, fetal-placental interface, bracket defines the hindgut lip (hgl). (**H**) Oblique frontal view, whole mount specimen, fetal-placental interface, initial DiI label applied to hgl (red, white arrow). (**I**) Specificity of DiI to hgl in a frontal optical section of the fetal-placental interface

(**I**) and a transverse slice through the hgl of the reconstructed z-stack (**J**). White dots (**I**) delineate the allantois; Dashed line (**J**) delineates allantoic cells from the hgl. (**K**) Right side view, whole mount specimen, DiI-labeled post-culture conceptus; fluorescent DiI visible within the midgut (mg) and hindgut (hg). (**L**) Oblique left-side view, DiI-labeled whole mount specimen after culture and photobleaching shows contribution to hg (brown, white arrow). (**M-P**) Transverse histological sections through fetal-placental interface (**M, N, P**) and allantois (**O**) showing cultured photobleached DiI-labeled (**M, N**) and unlabeled (**O, P**) specimens. Labeled specimens exhibit positive staining in the hg (**M, N**), notochord (nc, **M**), omphalomesenteric artery (oa, **M**) and splanchnic mesoderm (sm, **M**). Unlabeled photobleached control exhibits background staining limited to visceral endoderm (arrowhead in **P**); the allantois (**O**), hg (**P**), and other internal structures (**P**) exhibit no detectable staining. Scale bar (**P**): 10 μm (**A-F**); 20 μm (**J, G**); 40 μm (**M, O**); 50 μm (**N, P**); 75 μm (**H, I, K**); 100 μm (**L**); 145 μm (**K**). al, allantois; da, dorsal aortae; fg, foregut; hrt, heart; ua, umbilical artery; ys, yolk sac.

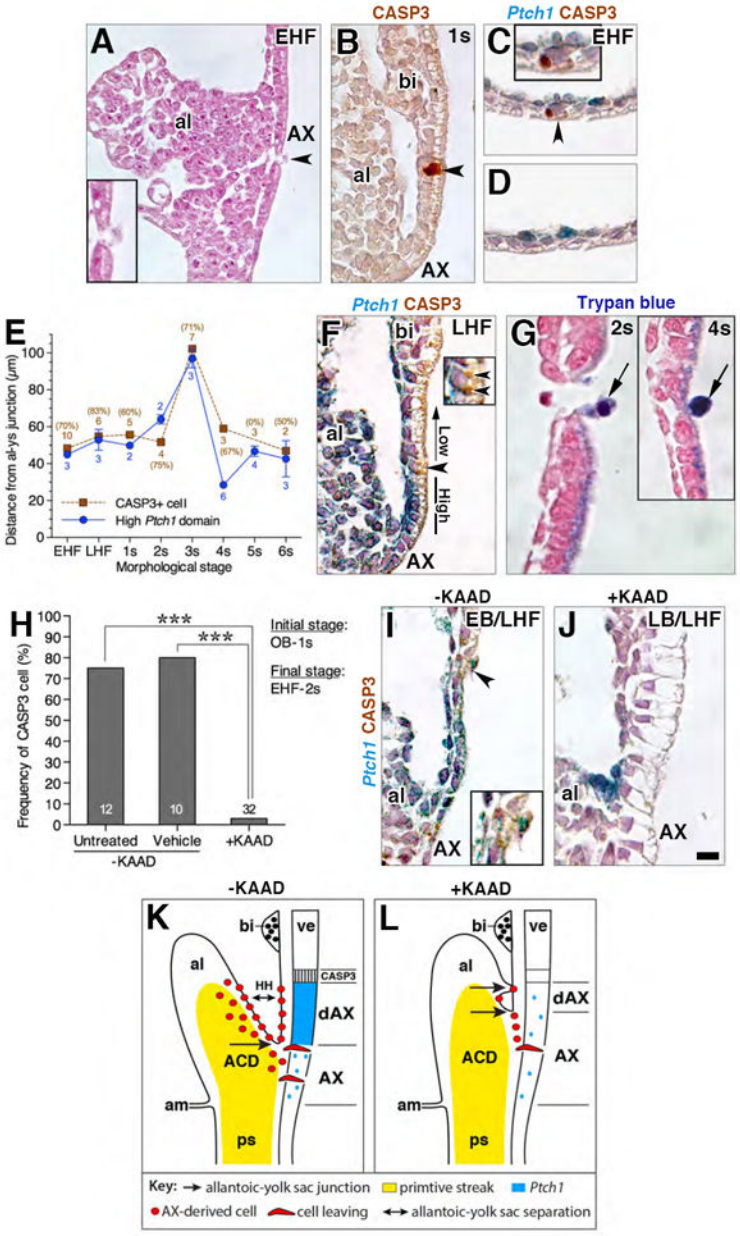

Figure 8. A single CASP3 cell, whose identity is regulated by Hedgehog signaling, separates non-EMT blood island visceral endoderm from the AX

(**A**) Sagittal histological section, allantois, showing breach in the AX (arrowhead; region enlarged in inset). Breaches are not due to dissection, as embryos in which overlying parietal endoderm remained intact exhibited them (data not shown). (**B**) Sagittal CASP3-immunostained histological section, allantoic-yolk sac interface, displaying a single CASP3-positive cell (arrowhead) at the distal border of the dAX. (**C, D**) Transverse CASP3-immunostained histological sections, distal junction of the dAX in a *Ptc:lacZ* reporter conceptus. The unique CASP3-positive cell (**C**, arrowhead; enlarged in inset) is axially located within the midline and does not span into the consecutive section (**D**). (**E**) Graph displaying the co-location of the CASP3-positive cell and distal limit of the high *Ptch1* dAX

domain as the distance from the allantoic-yolk sac junction at increasing morphological stages. Sample sizes next to data points, along with the frequency at which the CASP3-positive cell was found for each stage. (**F**) Sagittal CASP3-immunostained histological section through the allantoic-yolk sac interface in a *Ptc:lacZ* reporter, CASP3-positive cell (arrowhead; enlarged in inset with arrowheads) is located between the visceral endoderm's high *Ptch1* domain and the yolk sac blood islands. Apically-localized punctate staining is visible in the visceral endoderm; this staining was commonly observed in extraembryonic visceral endoderm in this study. (**G**) Sagittal histological sections, yolk sac, showing several examples of trypan blue cells (arrows) being extruded from the epithelium at a similar distance from the allantoic-yolk sac junction as the CASP3 border cell (data not shown). (**H**) Frequency of the CASP3-positive cell in control (-KAAD) and KAAD-treated (+KAAD) specimens, sample sizes, base of each bar. Significance: Fisher's exact test; ***, $P < 0.001$. (**I, J**) Sagittal CASP3-immunostained histological sections through the allantoic-yolk sac interface in cultured *Ptc:lacZ* reporter conceptuses; untreated (-KAAD, **I**), treated (+KAAD, **J**). While a CASP3-positive cell, just distal to the high *Ptch1* domain, is found in the control (**I**, arrowhead; enlarged in inset), no signs of the high *Ptch1* domain or the CASP3-positive cell are evident in the KAAD-treated specimen (**J**). (**K, L**) Schematic representation of the expanded AX domain in +KAAD specimens (**L**) relative to that in –KAAD (**K**). Scale bar (**J**): 9 μm (**G**); 15 μm (**G** inset, **J**); 20 μm (**B, F, I**); 25 μm (**A, C, D**). al, allantois; bi, blood island; hgl, hindgut lip.

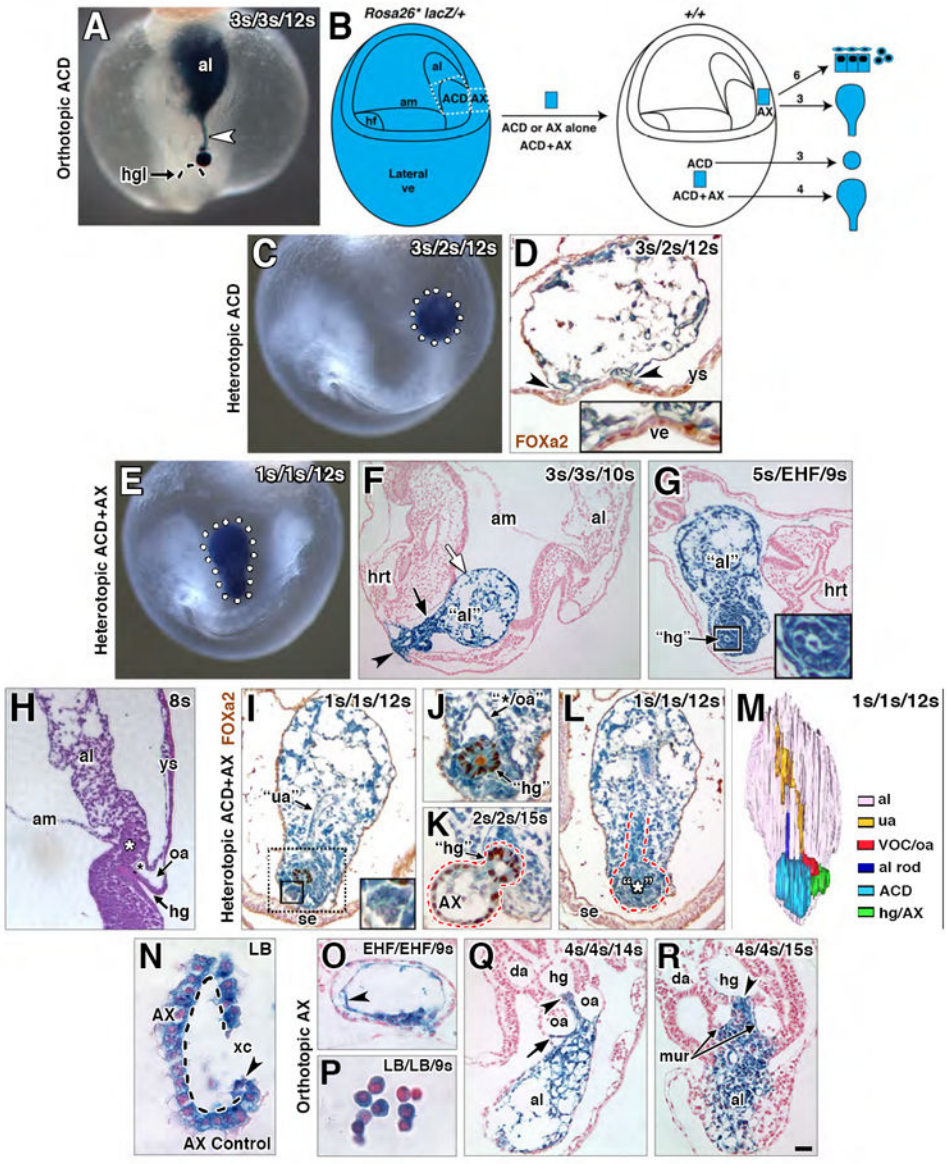

Figure 9. Potency testing and/or fate mapping the ACD, ACD+AX, and AX via grafting

(**A**) Orthotopic ("same site") ACD graft (blue) extending a midline file of cells (white arrowhead) from the hindgut lip (dashed arc) into the distal allantois. (**B**) Schematic diagram, grafting protocol. ACD, AX or ACD+AX were removed (white dashed regions) from a donor *Rosa26*/+* conceptus and grafted into an F2 host conceptus. Lateral visceral endoderm (ve) was chosen as the heterotopic site as it was fairly tissue-free. Arrows, right of the host conceptus, outcome of each graft type (see text). Numbers above arrows, sample sizes. (**C, D**) Heterotopically-grafted donor ACD "sphere" (blue, dotted white circle) within host post-culture. (**D**) Transversely-oriented FOXa-2-immunostained histological section, donor ACD, and its contact with the lateral ve (arrowheads, higher magnification of this region, inset). The ACD is apolar, filled with disorganized small vessels, and lacks any indication of hindgut formation and/or the dense core domain. (**E-G**) Heterotopically grafted ACD+AX post-culture, whole mount preparations (**E**), showing the elongated shape (white

dotted outline) of donor ACD+AX graft (blue). **F** and **G**, histological sections, integrated donor ACD+AX graft (**F**, blue, arrowhead), and a free-floating donor ACD+AX graft (**G**, blue color) within the host. Donor ACD+AX grafts resemble "stem-and-lollipop" structure of intact allantois and its connection to the hindgut; distal region loosely organized (white arrow, **F**); proximal region dense (black arrow, **F**) with a putative hindgut (boxed, **G**; enlarged in inset). (**H**) Sagittal histological section, fetal-placental interface, *ex vivo* conceptus showing the relationship between the distal and proximal regions in an intact conceptus. White asterisk, ACD; black asterisk, VOC. (**I-L**) FOXa-2-immunostained histological sections, heterotopic ACD+AX grafts (blue) post-culture. (**I**) Midline vessel, reminiscent of the umbilical artery ("ua"), runs through proximal half of the graft. At the proximal end (dotted black box), FOXa2-negative rosette formations (solid black box, enlarged in inset) are identified. (**J**) In the same specimen as (**I**), a single FOXa2-positive "hindgut" tube-like structure is adjacent to a large vessel, reminiscent of the VOC and/or omphalomesenteric artery ("*/oa"). (**K**) FOXa2 in the single "hindgut" structure and donor AX tissue (red dashed line). (**L**) Rod-like file of cells extends through the proximal midline of the graft from a dense core (red outline), reminiscent of the ACD (asterisk) and its rod-like extension. (**M**) 3-D model of free-floating graft whose colored structures are presented in panels **I, J,** and **L**. (**N**) Histological section through an uncultured control donor AX (dashed outline, basal side) clean of associated mesoderm. Arrowhead, apparent bilayer at this site is really the visceral endoderm curved on itself. (**O-R**) Histological sections through hosts and orthotopic AX grafts (blue) post-culture. (**O, P**) Bud and headfold-stage AX grafts, which failed to integrate into the hosts, formed squamous mesoderm (**O**, arrowhead) and a cluster of blood cells (**P**). (**Q, R**) Early somite-stage AX grafts, integrated into host, contributing to the allantois (**Q, R**), hindgut (**Q, R**, arrowhead), medial umbilical roots (mur, **R**), and the omphalomesenteric artery (oa) and overlying splanchnic mesoderm (**Q**, arrow). Scale bar (**R**): 10 μm (**N, P**); 20 μm (**J, O**); 30 μm (**K**); 40 μm (**D, H, I, L, Q**); 50 μm (**A, R**); 80 μm (**C, G**); 90 μm (**E, F**). al, allantois; am, amnion; da, dorsal aortae; hg, hindgut; hgl, hindgut lip; hrt, heart; mur, medial umbilical roots; oa, omphalomesenteric artery; se, surface ectoderm; ua, umbilical artery; VOC, vessel of confluence; ve, visceral endoderm; ys, yolk sac; xc, exocoelomic cavity.

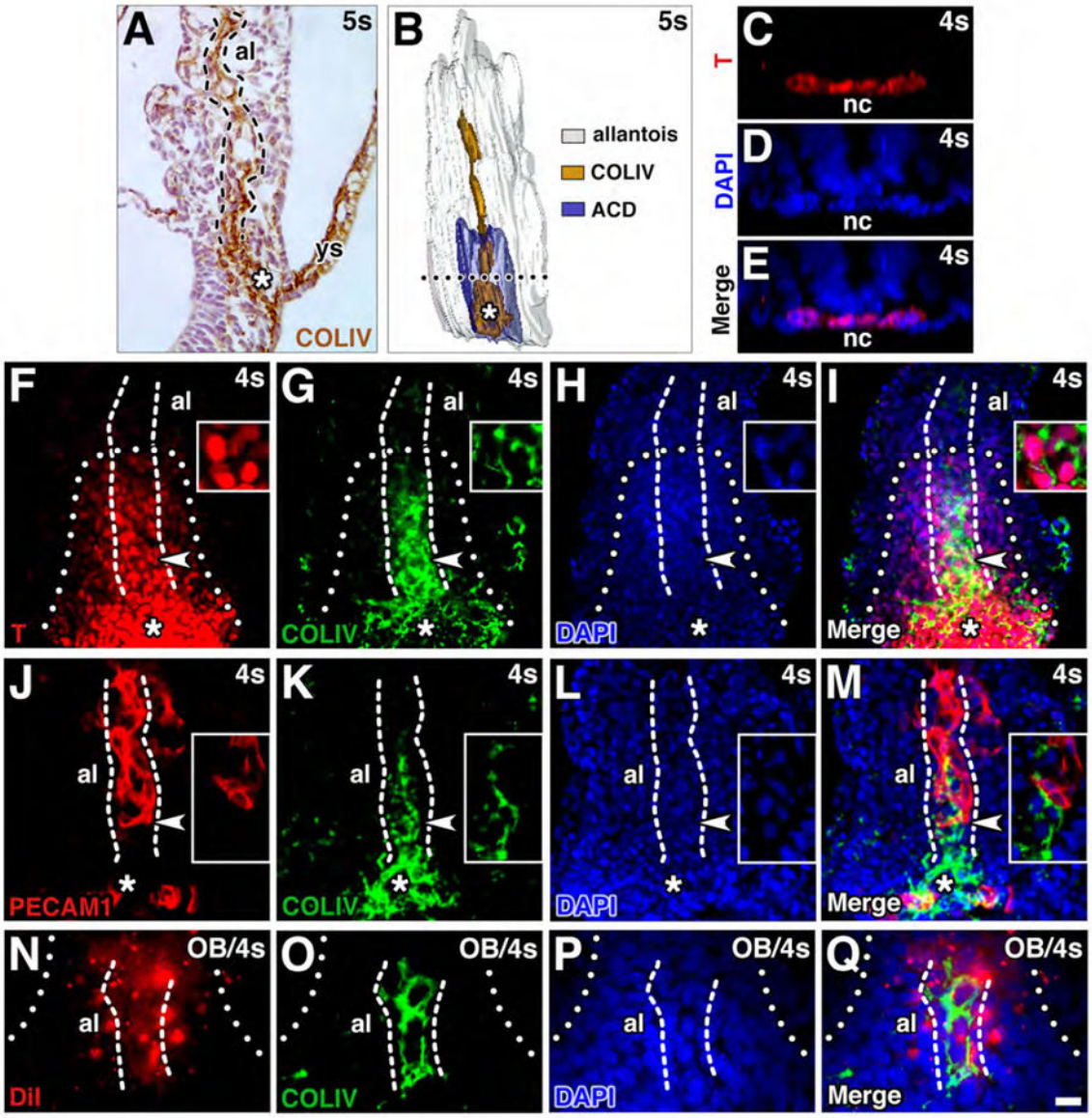

Figure 10. COLIV identifies the AX-derived allantoic rod

For all panels, the allantoic rod is encased by dashed lines and the proximal ACD is indicated with a white asterisk. (**A**) Sagittal COLIV-immunostained histological section, allantoic-yolk sac interface, displaying a rod-like file of COLIV extending from the dense proximal ACD through the allantoic midline. (**B**) Frontal (ventral) view, 3-D model reconstructed from serial sections of specimen in **A**; color key displayed. Dotted line delineates the base of the allantoic rod, which lies within the dense ACD. (**C-E**) Transverse slice, reconstructed z-stack of the anterior embryo. T localizes to and defines the embryonic notochord. (**F-I**) Frontal optical section through the allantois, showing the ACD defined by T (white dotted outline) and the allantoic rod defined by COLV. Insets: high magnification of rod at level of white arrowhead, showing COLIV surrounding T-positive cells. (**J-M**) Frontal optical section through the allantois, showing that the nascent umbilical artery defined by

PECAM1 is distinct from the COLIV rod. Insets: high magnification of region at level of white arrowhead. (**N-Q**) Frontal optical section through the allantois, the COLIV rod-like structure is encased with DiI, and thus derived from the AX. Scale bar (**Q**): 6 μm (**C-E, F-I** insets); 10 μm (**J-M** insets, **N-Q**); 15 μm (**J-M**); 20 μm (**F-I**); 35 μm (**A**). al, allantois; nc, notochord; ys, yolk sac.

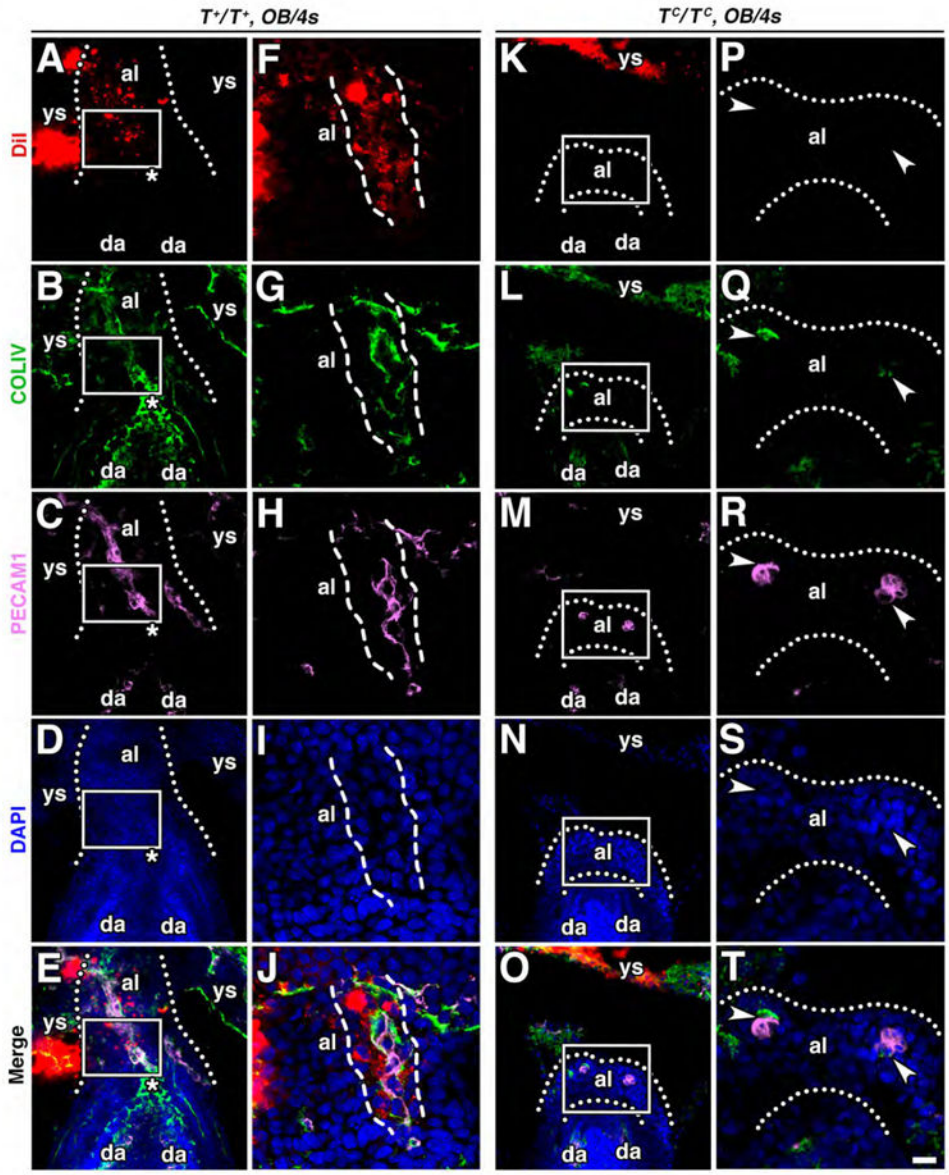

Figure 11. T^C/T^C mutant allantoises lack AX contribution and its derivative rod-like structure, which may organize the allantoic vasculature

For all panels, the allantoic rod and PECAM1 midline vessel are encased by dashed lines, the allantois is outlined by dotted lines, and the proximal ACD is indicated with a white asterisk. (**A-T**) Frontal optical sections through the fetal-placental interface of a wildtype T^+/T^+ allantois (**A-E**) and a T^C/T^C mutant allantois (**K-O**) aided by higher magnification views of the white-boxed allantoic region in all of these panels (**F-J, P-T**), showing AX contribution to the allantoic rod (**A-J**) and failure of the T^C/T^C mutants to form a rod (**K-T**). White arrowheads (**P-T**), disorganized clusters of PECAM1- and COLIV-positive cells. Scale bar (**T**): 10 μm (**F-J, P-T**); 35 μm (**A-E, K-O**). al, allantois; da, dorsal aortae; ys, yolk sac.

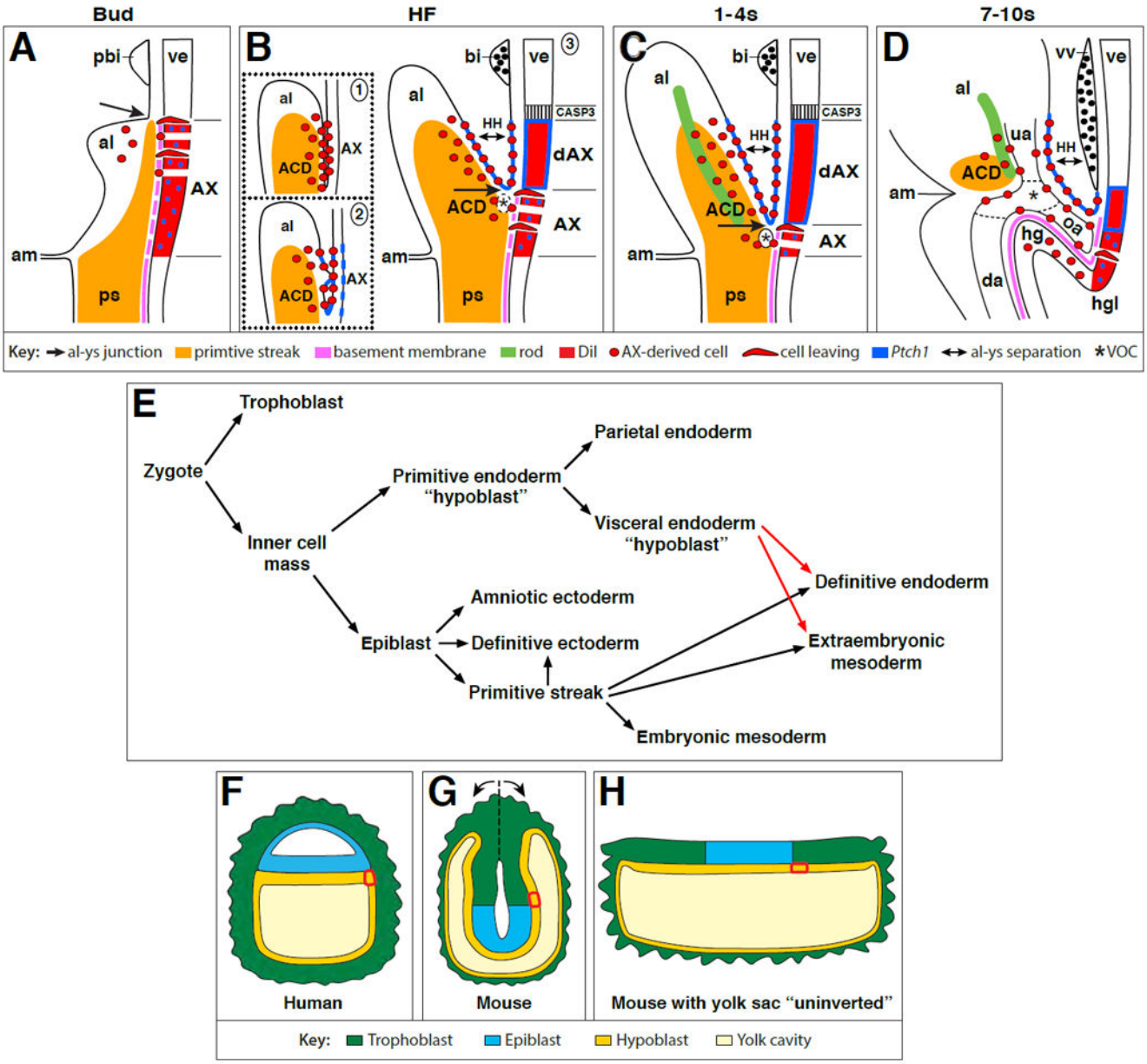

Figure 12. Exfoliation of AX leads to a revised mouse fate map and human comparison

(**A-D**) Schematic diagram depicting exfoliation of AX through the mid-sagittal plane (**A-C**; modified from (Rodriguez et al., 2017)), while the embryonic component in D is slightly laterally oriented to visualize one of the paired dorsal aortae. See text for details. (**E**) Revised mouse fate map (red arrows) shows AX contribution (visceral endoderm) to definitive endoderm (this study, and (Kwon et al., 2008)) and extraembryonic mesoderm (this study). (**F-H**) General schematic of the early post-implantation human (**F**) and mouse (**G**) conceptus; color key below. The mouse yolk sac has been "un-inverted" (**H**) by splitting the egg cylinder along the dashed line in **G** to flatten the epiblast in **H**, likening the mouse conceptus to that of the human (**F**). Small red box indicates the prospective AX of the mouse

and the site where the human yolk sac diverticulates to form the allantois/body stalk. al, allantois; am, amnion; bi, blood island; da, dorsal aortae; hg, hindgut; HH, Hedgehog signaling; oa, omphalomesenteric artery; pbi, prospective blood island; ps, primitive streak; ua, umbilical artery; ve, visceral endoderm; vv, vitelline vessels.